Effect of Erroneous Representation of Location and Orientation of EM Receivers for Monitoring of Submarine Petroleum Reservoirs

Master of Science Thesis in Applied Mathematics

Hanne Christine Seyffarth

Department of Mathematics
University of Bergen

June 2, 2009

Forord

Først og fremst vil jeg takke mine veiledere Trond Mannseth og Martha Lien for god hjelp og veiledning. Videre vil jeg takke mine venner og medstudenter for en fantastisk tid på instituttet. Jeg vil spesielt takke Hilde Kristine for at hun ikke ville begynne på master i matematikk uten meg. Møt meg på skalldyrfestivalen i Mandal eller i bassenget!

Contents

Chapter 1

Introduction

The request for improving the methods in the search of new hydrocarbon reservoirs and in optimizing the hydrocarbon production is very large. Since the quantity of undetected hydrocarbon reservoirs is decreasing, improvement of optimization techniques for production is of particular interest.

Production monitoring of reservoirs is important in this context, and will serve as motivation for the research presented in this thesis. Consider a reservoir which initially is completely filled with hydrocarbons. To increase the production rate, the pressure in the reservoir is increased by injecting saline water. This is illustrated in Figure 1.1 and Figure 1.2. As water is injected, a transition zone that separates the two fluids will appear. This transition zone will develop as the water pushes the hydrocarbons towards the production well. To design good production strategies, it is desirable

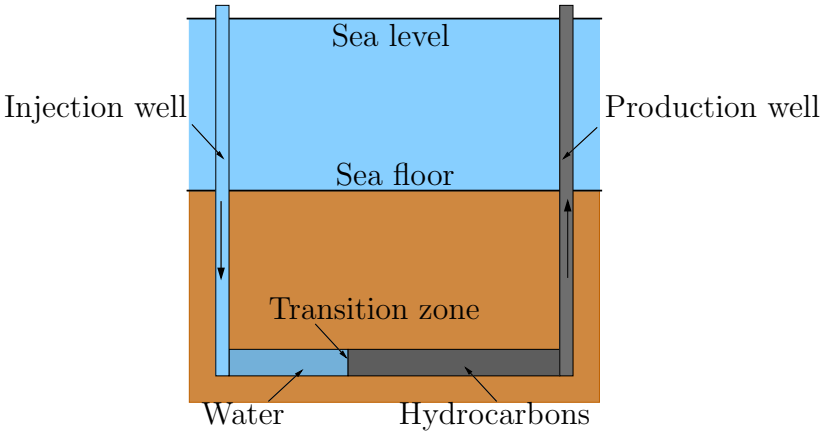

Figure 1.1: The simplified sketch shows how water is injected in order to push the hydrocarbons in the reservoir towards a production well.

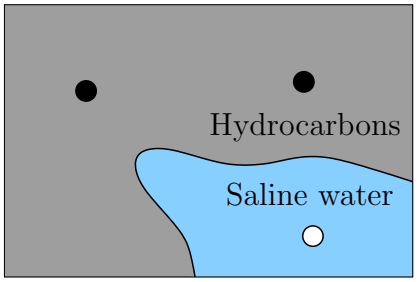

Figure 1.2: A simplified sketch of a reservoir that is pictured from above. In the white injection well, saline water is injected in order to displace the hydrocarbons towards the black production wells. The blue region is filled with saline water, the grey region is filled with hydrocarbons, and the black line in between them marks the transition zone.

to describe this evolution as accurately as possible. This is called reservoir production monitoring.

Commonly, seismic data are used in reservoir production monitoring. Seismic waves depend on the elastic properties of the medium in which it propagates. The elastic properties of a reservoir rock depend on the fluid saturation. Seismic methods utilize the difference in elastic properties of rock containing water and rock containing oil to locate the transition zone. However, there are some problems with this approach. Firstly, the volume of the water-filled region changes only slightly between each acquisition, and secondly, the difference in elastic properties is small. For these reasons the seismic signals will be weak. Furthermore, changes in pressure will also affect the elastic properties of the rock, and this may lead to complications.

Seismic monitoring of a flooding front is therefore a difficult task. One alternative approach is using electromagnetic data. Electromagnetic signals will be highly influenced by the electric conductivity of the rock. The difference in electric conductivity of a rock filled with hydrocarbons and rock filled with saline water is very large, and for successive acquisitions changes in the conductivity distribution of the reservoir may be detected. For this reason investigations concerning the use of electromagnetic data for monitoring have recently been performed (see e.g. Lien and Mannseth (2008), Orange et al. (2009)).

The receivers in electromagnetic monitoring should optimally be placed exactly in the same location during every single acquisition. However, for technological and economical reasons, the receivers are currently brought up to the surface to collect the measured data between each acquisition. This

demands repeatedly replacement of the receivers, and uncertainties in the location and the orientation of the receivers will thus arise. In this thesis we will perform an investigation of the sensitivity of the electromagnetic signal with respect to an erroneous representation of the location and orientation of the receivers. This will give an indication of whether solutions with fixed receivers should be used in the future.

In order to understand the behaviour of electromagnetic waves, we will in Chapter 2 discuss basic electromagnetic theory. Electromagnetic waves are governed by Maxwell's equations which are normally given in differential form. The technique we are going to apply in the numerical forward modelling is based on numerical implementation of Maxwell's equations in integral form.

Since electromagnetic waves are highly influenced by the electric conductivity of the medium in which it propagates, we will in Chapter 3 discuss the electric conductivity of reservoir rocks. The origin, composition, and internal structure of these rocks will therefore be considered, and the electric conductivity will by Archie's law be related to the fluid saturation and the wetting properties of the fluids. The saturation and the wetting properties of the fluids will be discussed in Chapter 4.

The fluid saturation obtained through electromagnetic surveys is usually compared to the saturation obtained through simulation of fluid flow. If the data do not correlate and there are errors in the simulated model, the measured saturation may be used in history matching. To give an overall picture, we will in Chapter 4 discuss flow in a reservoir rock. Since we in the current work study a reservoir under water-assisted production, the discussion will be restricted to flow of two fluids.

The use of electromagnetic waves for marine reservoir monitoring under water-assisted production will be considered in Chapter 5. Here the reference model for the forward modelling is presented, and uncertainties in the location and orientation of the receivers will be discussed.

In Chapter 6 we will consider the electromagnetic signal caused by a change in the electric conductivity of the subsurface. The effect of an erroneous representation of the location and orientation will be investigated, and the results from the numerical computations will be presented and discussed.

The results will be summarized in Chapter 7, and recommendations concerning repeatedly replacement of the receivers will be given.

Chapter 2

Electromagnetism

In this chapter we will start by discussing the basic theory of electricity and magnetism. The origin and behaviour of both electric and magnetic fields will be described, and we will discuss how the fields will affect various materials. After having discussed the two fields separately, interactions between them will be described, and electromagnetic waves will be discussed. We will further consider electromagnetic sources and receivers. The theory and illustrations are mainly based upon the books of Tipler and Mosca (2004), Tipler (1976), and Reitz et al. (1993).

The electromagnetic waves are governed by Maxwell's equations. Maxwell's equations will not be derived here. For the derivation of Maxwell's equations, see Maxwell (1864). Since Maxwell's equations normally are given in differential form, we will at the end of this chapter derive the integral form of Maxwell's equations. This derivation is mainly based upon the book of Zhdanov (2002).

2.1 Electricity

2.1.1 The Electric Charge

Atoms are the foundation of matter. Each atom has a tiny, but massive nucleus that contains protons and neutrons. Protons are positively charged, while neutrons are uncharged. The number of protons in the nucleus determines the type of atom and the atomic number of the element. Surrounding the nucleus is an equal number of negatively charged electrons. The hydrogen atom, H, illustrated in Figure 2.1 has one proton in the nucleus. Its atomic number is therefore one, and one electron orbits the nucleus. The proton is about 2000 times more massive than the electron. However, the charges of the

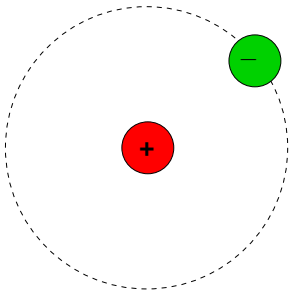

Figure 2.1: The hydrogen atom.

two particles are opposite, but equal in magnitude. The charge of the proton is e, and the charge of the electron is $-e$. The constant $e = 1.602177 \times 10^{-19}$ C is called the fundamental unit of charge, and C is the SI unit of charge called coulomb. This leaves the hydrogen atom with zero net charge. If an electron is removed or added to an atom, the number of electrons and protons will no longer be balanced. A net charge will thus arise. The charged atom is called an ion.

Atoms and ions are joined together to form molecules and materials. There are different kinds of bonds binding the atoms and ions, and the distribution of electrons will differ dependently on the binding mechanism. Some molecules are electrically neutral. This means that its intrinsic charges are balanced, which leaves the molecule with no net charge. We say that these molecules are non-polar. In other molecules this is not the case. As regards the water molecule, H_2O, it consists of two hydrogen atoms and one oxygen atom. Compared to the hydrogen atoms, the oxygen atom performs a higher attractive force on the electrons. This leaves the oxygen atom in the water molecule with a net negative charge, and the hydrogen atoms with a net positive charge. Because of the shape of the water molecule, the center of the negative charge does not coincide with the center of the positive charge. This leaves us with a system of two equal and opposite directed charges separated by a small distance. Such a system is called an electric dipole, and we say that the molecule is polar. The electric dipole for the water molecule is illustrated in Figure 2.2.

2.1.2 The Electric Field

Any charged particle produces an electric field everywhere in space. The eld will exert a force on any other charged particle. This means that when a particle with charge q is placed in an electric field, $\boldsymbol{E}$, it experiences a force,

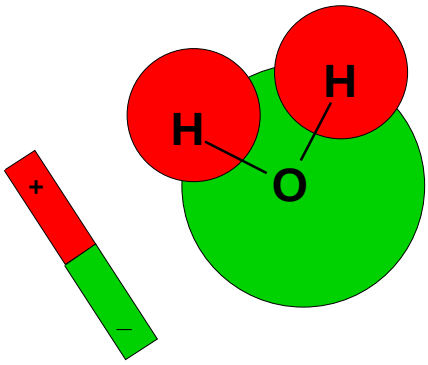

Figure 2.2: The distribution of charges in the water molecule.

$q\boldsymbol{E}$, which will cause an acceleration of the particle. Changes in the electric field propagates through space at the speed of light, c. This means that if a charge is suddenly moved, the force it exerts on a second charge does not change until some time later.

We may picture the electric field by drawing lines to indicate its direction. At any given point the field vector is tangent to these lines. The field lines always diverge from a particle that is positively charged and converge to a particle that is negatively charged. This is shown in Figure 2.3 and Figure 2.4. The number of field lines is proportional to the charge, q. As we move away from the charge, the electric field is weakened, and the field lines moves apart. The density of the field lines represents the strength of the field. The more closely spaced field lines, the stronger is the electric field.

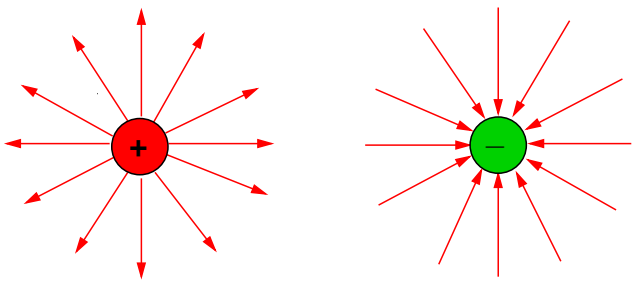

Figure 2.3: Visualization of the electric field lines of a positive and negative electric charge. Notice how the field lines diverge from the positive particle and converge to the negative particle.

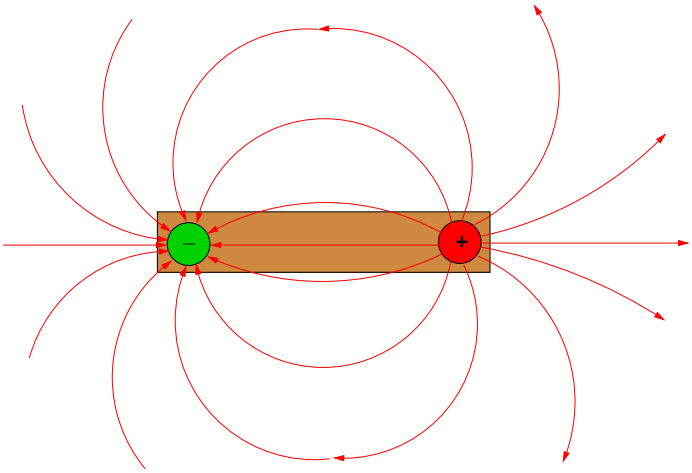

Figure 2.4: The field lines of an electric dipole. Notice how the field lines diverge from the positive charge and emerge at the negative charge.

2.1.3 Electricity in Matter

Since all materials are composed of charged particles, they will be affected by an external electric field. The kind of influence will depend on the composition of the material. Materials may be divided into two categories: conductors and insulators.

Conductors

Conductors are substances which contain a large number of charges that are free to move throughout the conducting material. Copper and other metals are examples of conductors. The movement of the electrons can be very complex. When no external electric field is present, the electrons move in random directions at a relatively high velocity. In addition, the electrons collide repeatedly with atoms, ions, and molecules in the material. Since the velocity vectors are randomly oriented, the average velocity is zero.

If an external electric field is applied, the field will exert a force on each charge. This force will cause a change in velocity in the direction opposite the field, and a flow of electrons is generated. The flow of electric charges constitutes an electric current, $\boldsymbol{j}$ which is defined as the amount of charge, Δq, flowing through a cross sectional area, A, per unit time, Δt. The SI unit of current is Ampere, and the direction of the current is considered to be the direction of flow of positive charges.

Because of the large amount of free charges in a conductor, the magnitude

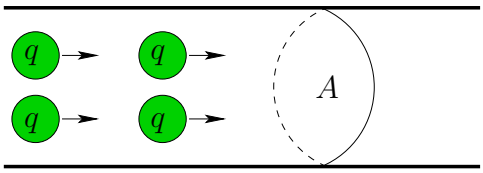

Figure 2.5: Illustration of an electric current through the cross sectional area, A.

of the electric current is high, and we say that the material has a high electric conductivity. The electric conductivity, σ, is a measure of the ability of a material to conduct electric currents. It is related to the electric current and the magnitude of the electric field by

$$\boldsymbol{j} = \sigma \boldsymbol{E} \, . \tag{2.1}$$

The electric conductivity depends on both the temperature and the composition of the material, and it is an intrinsic material property which is expressed in the reciprocal unit Siemens/meter (S/m).

Insulators

Insulators are substances in which all charged particles are bound strongly to constituent molecules. This means that within an ideal insulator, none of the charges are free to move. However, when an insulator is exposed to an external electric eld the positively charged particles will be forced in the direction of the electric eld, while the negatively charged particles are forced in the opposite direction. For this reason, the positive and negative parts of each molecule are displaced from their equilibrium positions in opposite directions, and the material is said to be polarized. The displacement of the charged particles is, however, limited. This is due to the strong bonds between the molecule and the charged particles. A polarized material is illustrated in Figure 2.6. Wood and glass are examples of insulators. The negatively charged electrons in wood and glass are bound to nearby atoms, and none of them are free to move. We will therefore have no flow of electric charges, and according to equation (2.1), the electric conductivity will be close to zero.

The polarized regions in the insulator produces electric fields. We call these fields the electric polarization, $\boldsymbol{P}$. The polarization of an insulator depends on the total electric field in the medium. This means that the electric polarization of one region depends on both the external electric field and the electric field which is produced by polarized regions in the material.

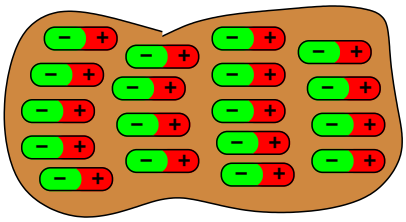

Figure 2.6: Illustration of a polarized insulator.

The net electric polarization of a material will make a contribution to the net electric field.

The Electric Displacement Field

We have seen that the electric conductivity of a conductor is high while that of an insulator is close to zero. Many materials have electric properties intermediate between conductors and insulators. When these materials are exposed to an external electric field, both electric polarization and electric currents may be generated. The magnitude of the electric current and the electric polarization of these materials will depend on the electric conductivity of the material. If the conductivity is low, the magnitude of the electric current will be relatively low while the magnitude of the polarization will be relatively high and vice versa. The electric conductivity will therefore affect how a material will respond to an external electric field.

We have seen that a material that is exposed to an external electric field will be influenced by this field. This influence depends on the electric conductivity of the material. If the material to some extent has been polarized by the external electric field, the electric polarization will make a contribution to the net electric field. It will therefore be convenient to define the electric displacement field, $\boldsymbol{D}$. The electric displacement field includes both a contribution from the source of the external electric field and a contribution from the polarization. It is given by

$$\boldsymbol{D} = \epsilon_0 \boldsymbol{E} + \boldsymbol{P} = \epsilon \boldsymbol{E} \, , \tag{2.2}$$

where ϵ_0 is the electric permittivity of free space, and ϵ is the electric permittivity of the material.

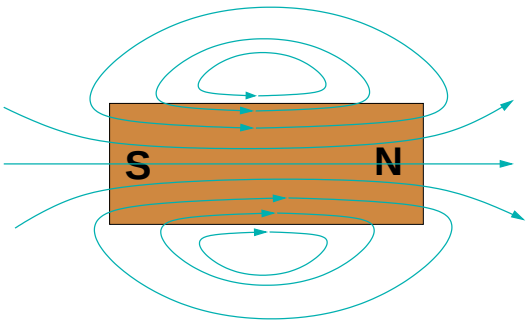

Figure 2.7: Magnetic field lines inside and outside a bar magnet. The lines emerge from the north pole and enter the south pole, but they have no beginning or end.

2.2 Magnetism

2.2.1 The Magnetic Field

As any charged particle induces an electric eld, any moving charged particle originates a magnetic eld. Just as the electric field may be represented by electric field lines, the magnetic field may be represented by magnetic field lines. In both cases, the direction of the field is indicated by the direction of the field lines, and the magnitude of the field is represented by their density.

There are, however, two important differences between electric field lines and magnetic field lines. Firstly, the direction of the electric field lines are in the direction of the electric force on a positive charge. The magnetic field lines, however, are perpendicular to the magnetic force on a moving charge. Secondly, the electric field lines begin on positive charges and end on negative charges while the magnetic field lines neither begin nor end.

Figure 2.7 shows the magnetic field lines both inside and outside a bar magnet. Magnetic poles in a magnet always occur in pairs.

2.2.2 Magnetism in Matter

In the section of electricity we learned that every atom consists of protons and electrons which are charged particles. Each electron is at any time circling around the nucleus of the atom in various kinds of orbits with a certain velocity. In addition it is spinning about its own axis. Since a movement of a charged particle originates a magnetic field, an atom may have a magnetic moment due to motion and spin of its electrons. The net magnetic moment of an atom depends on the alignment of the magnetic moments within the atom.

Similarly the magnetic moment of a material depends on the alignment of the magnetic moments of the atoms and molecules.

When a material is exposed to an external magnetic field, $\boldsymbol{H}$, the magnetic moments tend to align with the field. We say that the material is magnetized. A magnetized material is described by its magnetization, $\boldsymbol{M}$, which is defined as the net magnetic dipole moment per unit volume of the material. We may write the magnetization of a material as

$$\boldsymbol{M} = \chi_m \boldsymbol{H} \ ,$$

where the magnetic susceptibility, χ_m, is a measure of the ability of the material to magnetize. Based on the ability to magnetize, we may classify materials into the categories paramagnetic, ferromagnetic and diamagnetic.

Paramagnetism

In paramagnetic materials the magnetic dipoles do not interact strongly with each other and are normally randomly oriented. The magnetic susceptibility of a paramagnetic material is a small, positive number that depends on the temperature.

In the presence of an external magnetic field the dipoles will be partially aligned in the direction of the field. For this reason the paramagnetic material will obtain a small, positive magnetization which will increase the net, magnetic field. The degree of magnetization depends on the strength of the external field. However, while exposed to an external magnetic field of ordinary strength and at ordinary temperatures, only a very small fraction of the magnetic moments will align and the magnetization is therefore very small. This is because thermal motion tends to randomize their orientation.

Ferromagnetism

In a ferromagnetic material the magnetic dipole moments of the atoms exert strong forces on their neighbours. As a result, the magnetic moments over a small region, called a domain, will be aligned with each other even if the material is not exposed to an external field. Although the magnetic moments in each domain are aligned, the direction of alignment may vary from domain to domain. The ferromagnetic material will therefore not necessarily possess a net magnetic moment in the absence of an external magnetic field. However, if the ferromagnetic material possesses a net magnetic moment, we call the material a permanent magnet. The susceptibility of ferromagnetic materials is not a constant, and its maximum value may range from 5000 to 10000. In the case of permanent magnets, the susceptibility is not even defined. The

reason is that permanent magnets exhibit magnetization even in the absence of an external magnetic field.

On the other side, if a ferromagnetic material is exposed to an external magnetic field the boundaries of the domains shift, and the direction of alignment within a domain will change so that there is a net magnetic moment in the direction of the applied field. The degree of alignment is large even for small magnetic fields. Consequently, the magnetization of an ferromagnetic material is large, and the contribution to the net magnetic field will be large.

Diamagnetism

For diamagnetic materials, the magnetic dipole moments are in general randomly aligned. The magnetic susceptibility of a diamagnetic material is a small, negative constant that is independent of the temperature.

When a diamagnetic material is exposed to an external magnetic field, magnetic moments of opposite direction to the field will be induced. The material will therefore obtain a small, negative magnetization which will make a small, negative contribution to the net magnetic field. Thus the net magnetic field is decreased by the magnetization of a diamagnetic material. This diamagnetic behaviour occurs in all materials, but it is often weak and masked by paramagnetic or ferromagnetic behaviour. Diamagnetism is therefore observed only in materials whose molecules have no permanent magnetic moments.

The Magnetic Induction Field

We have now seen that a material will be magnetized while exposed to an external magnetic field. Since the magnetization will make a contribution to the net magnetic field, it will be convenient to introduce the magnetic induction field, $\boldsymbol{B}$. While the magnetic field only depends on the source of the external field, the magnetic induction field also depends on the nature of the medium present. The magnetic induction field thus includes the magnetization of the material, and it is related to the magnetic field by

$$\boldsymbol{B} = \mu_0(1 + \chi_m)\boldsymbol{H} = \mu\boldsymbol{H} \ , \tag{2.3}$$

where μ_0 is the magnetic permeability of free space and μ is the magnetic permeability of the material. Free space is a theoretically perfect vacuum, and the magnetic permeability of free space is dened by the constant value

$$\mu_0 \stackrel{def}{=} 4\pi \times 10^{-7} N/A \ .$$

Similarly to magnetic susceptibility, the magnetic permeability of a material describes how easily the material is magnetized by an external magnetic eld.

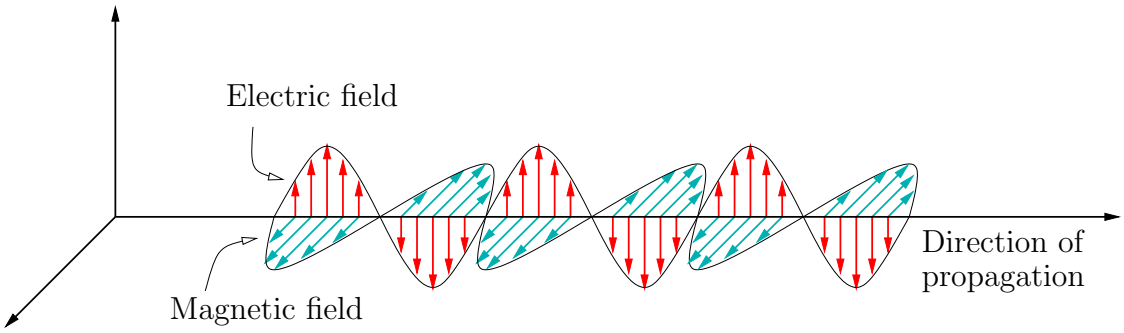

Figure 2.8: The electric and magnetic field vectors in an electromagnetic wave. The fields are in phase, perpendicular to each other, and perpendicular to the direction of propagation.

2.3 Electromagnetic Waves and Maxwell's equations

The electric and magnetic fields are closely connected, and a change in one of them will cause an induction of the other one.

2.3.1 Electromagnetic Waves

When free charges are accelerated, alternating electric and magnetic fields will be generated. The fluctuations in the electric and magnetic fields constitute an electromagnetic wave. The fields are in phase, and they are perpendicular to each other and to the direction of propagation. In vacuum the wave moves out away from the source at the speed of light. Consider the planar electromagnetic wave in Figure 2.8. An electromagnetic wave is planar if the direction of propagation is planar.

Normally, the electromagnetic waves are not planar. Let us now in Figure 2.9 consider an electromagnetic wave which is generated by an oscillating electric dipole. Since the propagation of an electromagnetic wave is perpendicular to the fields, we notice that this wave will propagate radially out away from the source. It is therefore not a planar wave. However, at great distances from the source the direction of propagation of the electromagnetic wave will approximately be planar. This means that at great distances from the source, the electromagnetic wave may be considered to be planar. The direction of propagation of such a electromagnetic wave is illustrated by Figure 2.10

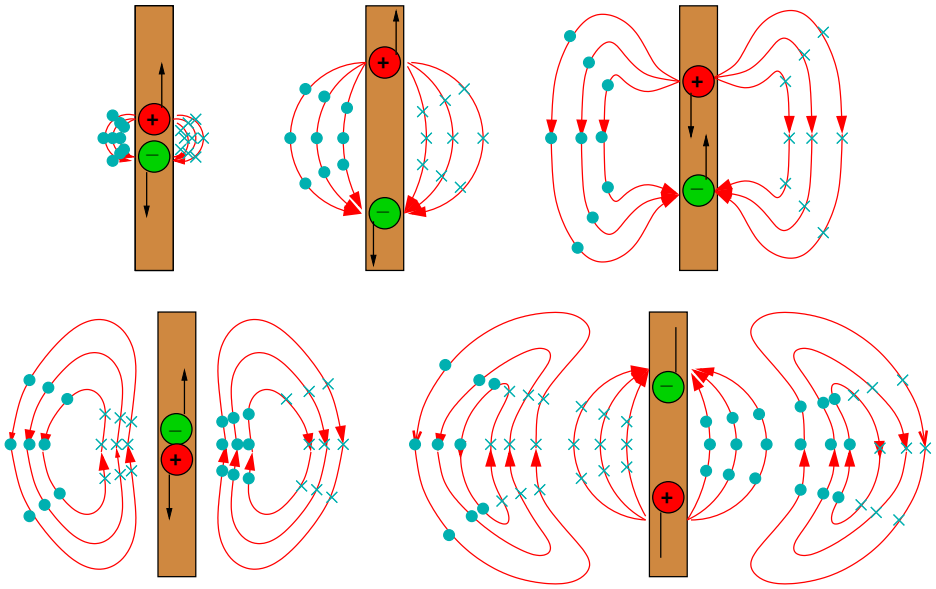

Figure 2.9: The electric and magnetic field lines produced by an oscillating electric dipole. The red lines are the electric field lines, while the blue dots and crosses illustrate the magnetic field lines. The dots represent arrows coming out of the paper, and the crosses represent arrows going into the paper. We notice how the electromagnetic wave propagates radially out away from the source.

Electromagnetic Receivers

The electric field in an electromagnetic wave of radio frequencies can be detected by an electric dipole antenna that is placed parallel to the electric field of the incoming wave. Then the electric field will induce an alternating current in the antenna. This current is measured, and thus we may determine the electric field. An electric dipole antenna is illustrated in Figure 2.11. In Chapter 5, we will consider electric dipole antennas in more details.

The magnetic field can be detected by a loop antenna placed perpendicular to the magnetic field. Changes of the magnetic flux through the loop will induce a current in the loop which will be measured. We may thus determine the magnetic field. A magnetic receiver is illustrated in Figure 2.12.

2.3.2 Maxwell's equations

The Scottish physicist James Clerk Maxwell first proposed the fundamental equations of electromagnetism, later known as Maxwell's equations. They relate the electric and magnetic field vectors and their sources. The sources

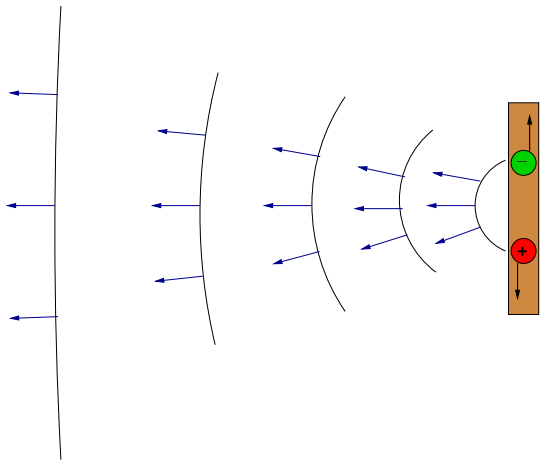

Figure 2.10: The blue arrows show the direction of propagation of an electromagnetic wave. Notice that near the source the direction of propagation is radial. Away from the source, the direction of propagation will become more and more planar.

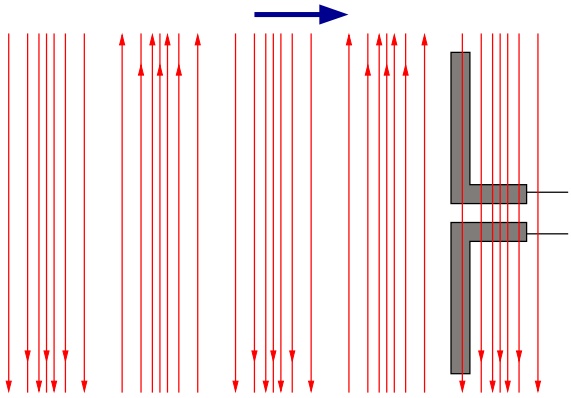

Figure 2.11: The electric field lines of a planar electromagnetic wave are illustrated together with an electromagnetic dipole antenna in the figure.

of electric and magnetic fields are, as discussed in the previous sections, electric charges and currents respectively. Maxwell's equations consist of the generalized Ampere's law (2.4), Faraday's law (2.5), Gauss' law (2.6), and

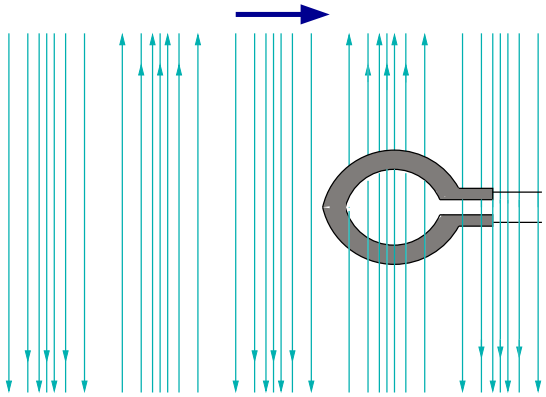

Figure 2.12: The magnetic field lines in a planar electromagnetic wave are shown together with an magnetic receiver.

Coulomb's law (2.7):

$$\nabla \times \boldsymbol{H} = \boldsymbol{j} + \boldsymbol{j}^e + \frac{\partial \mathbf{D}}{\partial t} , \tag{2.4}$$

$$\nabla \times \boldsymbol{E} = -\frac{\partial \boldsymbol{B}}{\partial t} , \tag{2.5}$$

$$\nabla \cdot \boldsymbol{B} = 0 , \tag{2.6}$$

$$\nabla \cdot \boldsymbol{D} = \boldsymbol{q} + \boldsymbol{q}^e . \tag{2.7}$$

Here $\boldsymbol{j}$ is electric current, $\boldsymbol{j}^e$ is extraneous electric current, $\boldsymbol{q}$ is the spatial density of free electric charges, and $\boldsymbol{q}^e$ is density of extraneous charges. The parameters are shown in Figure 2.13 for an electromagnetic wave that propagates through a medium 1.

The electric currents and charges are interrelated by the continuity equation

$$\nabla \cdot (\boldsymbol{j} + \boldsymbol{j}^e) = -\frac{\partial (\boldsymbol{q} + \boldsymbol{q}^e)}{\partial t} .$$

This equation expresses the fact that the divergence of electric currents from an infinitesimal volume is equal to the rate of decrease of electric charge density with time.

For a linear and isotropic medium we have the relations

$$\boldsymbol{D} = \varepsilon \boldsymbol{E}, \tag{2.8}$$

$$\boldsymbol{B} = \mu \boldsymbol{H}, \tag{2.9}$$

$$\boldsymbol{j} = \sigma \boldsymbol{E} , \tag{2.10}$$

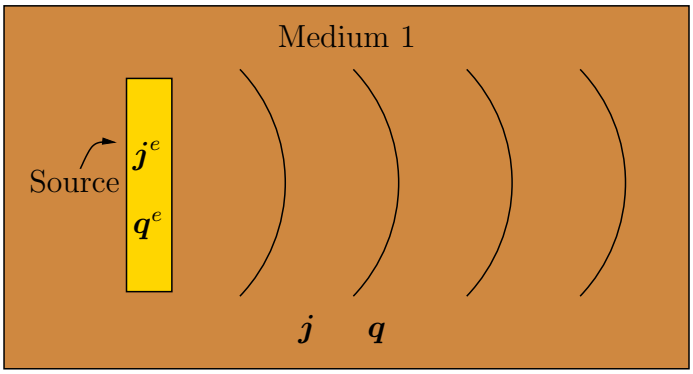

Figure 2.13: The parameters for an electromagnetic wave which is generated by a source and propagates through a medium 1.

where ε is the electric permittivity, μ is the magnetic permeability, and σ is the electric conductivity of a medium. By substitution of equations (2.8)-(2.10) into Maxwell's equations (2.4)-(2.7), we obtain

$$\begin{aligned} \bigtriangledown \times \boldsymbol{H} &= \sigma \boldsymbol{E} + \boldsymbol{j}^e + \varepsilon \frac{\partial \mathbf{E}}{\partial t} , \\ \bigtriangledown \times \boldsymbol{E} &= -\mu \frac{\partial \boldsymbol{H}}{\partial t} , \\ \bigtriangledown \cdot \boldsymbol{H} &= 0 , \\ \bigtriangledown \cdot \boldsymbol{E} &= \frac{\boldsymbol{q} + \boldsymbol{q}^e}{\varepsilon} . \end{aligned}$$

2.3.3 Derivation of the Integral Form of Maxwell's Equations

As mentioned in Chapter 1, we will in this study perform an electromagnetic forward modelling in order to investigate the sensitivity of electromagnetic data for monitoring. There are several techniques available for forward electromagnetic modelling. We will use a technique which is based on numerical implementation of the integral form of Maxwell's equations.

The main advantage of integral equation methods in comparison with differential equation methods is the fast and accurate simulation of the electromagnetic response in models with compact 2-D or 3-D bodies in a layered background. This method may also handle more complex models, but due to a large and dense matrix which arises in the integral equation formulation, the demand on computer resources is tremendous. The use of the integral equation method may therefore be limited in such cases.

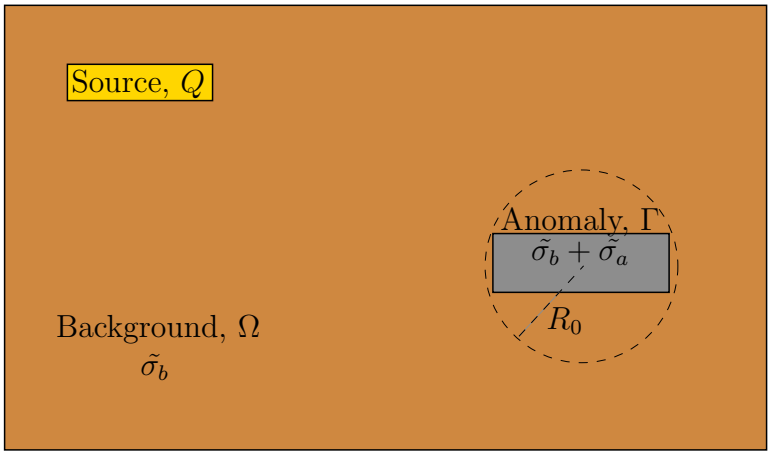

Figure 2.14: A visualization of the geoelectrical model. We have an electromagnetic source with current distribution Q which generates an electromagnetic wave. The region, Γ, of anomalous conductivity is consider to be local. This means that there exists a radius R_0 so that for $\sqrt{x^2 + y^2 + z^2} > R_0$ the medium has the background conductivity $\tilde{\sigma}_b$.

Assumptions

Let us from now on consider the 3-D geoelectrical model which is illustrated in Figure 2.14. For convenience the complex conductivity is defined as

$$\tilde{\sigma} = \sigma - i\omega\varepsilon \ , \tag{2.11}$$

where ω is the angular frequency and i is the imaginary unit. The figure shows a background, Ω, with the complex conductivity distribution $\tilde{\sigma}_b$. Embedded in the background we find a region of anomalous conductivity. We call this region the anomaly, Γ, and the difference in complex conductivity distribution between the anomaly and the background is called $\tilde{\sigma}_a$. We may write the complex conductivity, $\tilde{\sigma}$, as the sum

$$\tilde{\sigma} = \tilde{\sigma}_b + \tilde{\sigma}_a \ ,$$

The region of anomalous conductivity is considered to be local. This means that there exists some radius R_0 such that for $\sqrt{x^2 + y^2 + z^2} > R_0$, the medium has the background conductivity $\tilde{\sigma}_b$.

An external source with a current distribution, Q, generates a harmonic, electromagnetic field which propagates outwards. The field will propagate through the background and the anomaly. Both the background and the anomaly are assumed to be nonmagnetical, and both the density of the free,

electric charges and the density of the extraneous free charges is assumed to be zero. This means that the magnetic permeability of both the background and the anomaly equals the magnetic permeability of free space, $\mu = \mu_0 = 4\pi \times 10^{-7}$ H/m, and that $\boldsymbol{q} = \boldsymbol{q}^e = 0$.

Field Equations

Based on the assumptions, the electromagnetic field is described by the following equations in the time domain

$$\begin{aligned} \bigtriangledown \times \boldsymbol{H} &= \sigma \boldsymbol{E} + \boldsymbol{j}^e + \varepsilon \frac{\partial \mathbf{E}}{\partial t} \,, \\ \bigtriangledown \times \boldsymbol{E} &= -\mu_0 \frac{\partial \boldsymbol{H}}{\partial t} \,, \\ \bigtriangledown \cdot \boldsymbol{H} &= 0 \,, \\ \bigtriangledown \cdot \boldsymbol{E} &= 0 \,. \end{aligned}$$

By using Fourier transform, we obtain the equations in the frequency domain,

$$\bigtriangledown \times \boldsymbol{H} = \sigma \boldsymbol{E} + \boldsymbol{j}^e - i\omega\varepsilon \mathbf{E} = \tilde{\sigma} \boldsymbol{E} + \boldsymbol{j}^e \,, \tag{2.12}$$

$$\bigtriangledown \times \boldsymbol{E} = i\mu_0 \omega \boldsymbol{H} \,, \tag{2.13}$$

$$\bigtriangledown \cdot \boldsymbol{H} = 0 \,, \tag{2.14}$$

$$\bigtriangledown \cdot \boldsymbol{E} = 0 \,. \tag{2.15}$$

In order to derive the integral form of Maxwells equations, it will be an advantage to nd two equations describing the electric and magnetic elds separately. We will therefore rewrite the equations (2.12) - (2.15). By substituting equation (2.13) into equation (2.12), we obtain

$$\bigtriangledown \times (\frac{1}{i\mu_0\omega} \bigtriangledown \times \boldsymbol{E}) = \tilde{\sigma} \boldsymbol{E} + \boldsymbol{j}^e \,,$$

which is an equation of the electric field only. Since μ_0 and ω are constant in space, we get

$$\frac{1}{i\mu_0\omega} \bigtriangledown \times \bigtriangledown \times \boldsymbol{E} = \tilde{\sigma} \boldsymbol{E} + \boldsymbol{j}^e \,.$$

If we remember the vector identity

$$\bigtriangledown \times \bigtriangledown \times \boldsymbol{E} = \bigtriangledown \bigtriangledown \cdot \boldsymbol{E} - \bigtriangledown^2 \boldsymbol{E} \,,$$

and recall the equation (2.15), we find

$$-\frac{1}{i\mu_0\omega} \bigtriangledown^2 \boldsymbol{E} = \tilde{\sigma} \boldsymbol{E} + \boldsymbol{j}^e.$$

We obtain the expression

$$\bigtriangledown^2 \boldsymbol{E} + i\mu_0\omega\tilde{\sigma}\boldsymbol{E} = -i\mu_0\omega\boldsymbol{j}^e, \tag{2.16}$$

which is the wave equation of the electric field. In a similar procedure we find the wave equation,

$$\bigtriangledown^2 \boldsymbol{H} + i\mu_0\omega\tilde{\sigma}\boldsymbol{H} = -\bigtriangledown \times \boldsymbol{j}^e \ , \tag{2.17}$$

for the magnetic field.

Equations for the Anomalous Fields and the Background Fields

We have seen that the complex conductivity can be written as the sum

$$\tilde{\sigma} = \tilde{\sigma_b} + \tilde{\sigma_a} \ .$$

Correspondingly we can write the electric and the magnetic fields, $\boldsymbol{E}$ and $\boldsymbol{H}$, as a sum of the background and the anomalous fields

$$\begin{aligned} \boldsymbol{E} &= \boldsymbol{E}^a + \boldsymbol{E}^b \ , \\ \boldsymbol{H} &= \boldsymbol{H}^a + \boldsymbol{H}^b \ . \end{aligned}$$

The subscripts a and b denote the anomalous and the background fields respectively.

For simplicity we will from now on consider the electric z-component only. However, the procedure is similar for the other components. The z-component of equation (2.16) is

$$\bigtriangledown^2 E_z + i\mu_0\omega\tilde{\sigma}E_z = -i\mu_0\omega j_z^e \ , \tag{2.18}$$

We may use equation (2.18) to deduce expressions for the background field for the electric z-component

$$\bigtriangledown^2 E_z^b + i\mu_0\omega\tilde{\sigma_b}E_z^b = -i\mu_0\omega j_z^e \ . \tag{2.19}$$

By subtracting equation (2.19) from equation (2.18), we will find the expression for the anomalous field

$$\bigtriangledown^2 E_z^a + i\mu_0\omega\tilde{\sigma_b}E_z^a = -i\mu_0\omega j_z^\Gamma \ . \tag{2.20}$$

Here j_z^Γ can be understood as the excess current flowing in the inhomogeneous region, Γ. It is related to E_z by

$$j_z^\Gamma(\boldsymbol{r}) = \tilde{\sigma}_a(\boldsymbol{r})E_z(\boldsymbol{r}) = \tilde{\sigma}_a(\boldsymbol{r})(E_z^a(\boldsymbol{r}) + E_z^b(\boldsymbol{r})) \ . \tag{2.21}$$

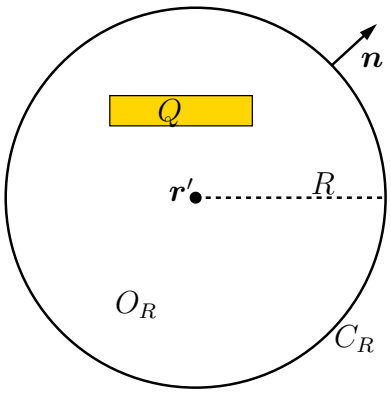

Figure 2.15: We have drawn a circle, C_R, with radius R about the arbitrary point $\boldsymbol{r}'$. The current distribution, Q, falls within the region O_R which is bound by the circle C_R.

Green's Function

Green's function, $G_b(\boldsymbol{r}'|\boldsymbol{r})$, for the background model is important in the derivation of Maxwell's equations in integral form. It depends on the position of the two points $\boldsymbol{r}$ and $\boldsymbol{r}'$ in space. Green's function of the electric z-component is determined by a solution of the equation

$$\bigtriangledown^2 G_b^{E_z}(\boldsymbol{r}'|\boldsymbol{r}) + i\mu_0\omega\tilde{\sigma}_b G_b^{E_z}(\boldsymbol{r}'|\boldsymbol{r}) = -i\mu_0\omega\delta(\boldsymbol{r}' - \boldsymbol{r}) \; . \tag{2.22}$$

The solution of this equation tends to zero at infinity, and the Dirac delta function, δ, is defined as

$$\iiint_O f(\boldsymbol{r})\delta(\boldsymbol{r}' - \boldsymbol{r})d\boldsymbol{x} = \begin{cases} f(\boldsymbol{r}') & \text{if } \boldsymbol{r}' \in D \\ 0 & \text{if } \boldsymbol{r}' \notin \bar{D} \; . \end{cases}$$

Here $f(\boldsymbol{r})$ is an arbitrarily continuous function in some domain D, and $\bar{D}$ includes the closure of D, i.e. $\bar{D} = D + S$, when S is the boundary surface of the domain D.

We will now select an arbitrary point $\boldsymbol{r}'$ and draw a circle, C_R, around it with a radius large enough for Q to fall within the region O_R bounded by the surface C_R. This means that $Q \subset O_R$. We then write Green's theorem for the background field of electric z-component, E_z^b, within the region of O_R as

$$\iiint_{O_R} [E_z^b \bigtriangledown^2 G_b^{E_z} - G_b^{E_z} \bigtriangledown^2 E_z^b]d\boldsymbol{r} = \iint_{C_R} [E_z^b \frac{\partial G_b^{E_z}}{\partial \boldsymbol{n}} - G_b^{E_z} \frac{\partial E_z^b}{\partial \boldsymbol{n}}]dS \; . \tag{2.23}$$

Here $E_z^b = E_z^b(\boldsymbol{r})$, $G_b^{E_z} = G_b^{E_z}(\boldsymbol{r}'|\boldsymbol{r})$, and $\frac{\partial}{\partial \boldsymbol{n}}$ denotes the directional derivative in the direction of the external unit vector, $\boldsymbol{n}$, normal to the surface C_R.

By substituting equation (2.19) and (2.22) into equation (2.23) and using the definition of the Dirac delta function, we obtain

$$i\omega\mu_0 \iiint_Q G_b^{E_z} j_z^e d\boldsymbol{r} - \iint_{C_R} [E_z^b \frac{\partial G_b^{E_z}}{\partial \boldsymbol{n}} - G_b^{E_z} \frac{\partial E_z^b}{\partial \boldsymbol{n}}] dS = i\omega\mu_0 E_z^b(\boldsymbol{r}') \ .$$

According to the radiation conditions, the functions E_z^b and G_b decrease as $\frac{1}{\sqrt{\boldsymbol{r}}}$ as $|\boldsymbol{r}| \to \infty$. Consequently if the radius, R, is expanded without limit, the surface integral along C_R will tend to zero, and we find

$$E_z^b(\boldsymbol{r}') = \iiint_Q G_b^{E_z}(\boldsymbol{r}'|\boldsymbol{r}) j_z^e(\boldsymbol{r}) d\boldsymbol{r} \ .$$

As mentioned, we may in a similar manner derive integral equations for every component of the electric and magnetic anomalous and background field. We will then obtain the system of equations

$$\boldsymbol{E}^b(\boldsymbol{r}') = \iiint_Q \boldsymbol{G}_b^{\boldsymbol{E}}(\boldsymbol{r}'|\boldsymbol{r}) \boldsymbol{j}^e(\boldsymbol{r}) d\boldsymbol{r} \ , \tag{2.24}$$

$$\boldsymbol{H}^b(\boldsymbol{r}') = \iiint_Q \boldsymbol{G}_b^{\boldsymbol{H}}(\boldsymbol{r}'|\boldsymbol{r}) \boldsymbol{j}^e(\boldsymbol{r}) d\boldsymbol{r} \ , \tag{2.25}$$

$$\boldsymbol{E}^a(\boldsymbol{r}') = \iiint_\Gamma \boldsymbol{G}_b^{\boldsymbol{E}}(\boldsymbol{r}'|\boldsymbol{r}) \tilde{\sigma}_a(\boldsymbol{r}) (\boldsymbol{E}^a(\boldsymbol{r}) + \boldsymbol{E}^b(\boldsymbol{r})) d\boldsymbol{r} \ , \tag{2.26}$$

$$\boldsymbol{H}^a(\boldsymbol{r}') = \iiint_\Gamma \boldsymbol{G}_b^{\boldsymbol{H}}(\boldsymbol{r}'|\boldsymbol{r}) \tilde{\sigma}_a(\boldsymbol{r}) (\boldsymbol{E}^a(\boldsymbol{r}) + \boldsymbol{E}^b(\boldsymbol{r})) d\boldsymbol{r} \ . \tag{2.27}$$

Here $\boldsymbol{G}_b^{\boldsymbol{E}}$ and $\boldsymbol{G}_b^{\boldsymbol{H}}$ is respectively Green's tensors for the background electric and magnetic fields. The equations (2.24) to (2.27) will be the basis for the IE modelling method.

Chapter 3

Physics of Rocks

In this chapter, we will discuss typical host rocks for fluids. As a host rock, the rock needs some empty space available for fluids. Many sedimentary rocks possess such a property. This is due to their origin. Since more than 5/6 of the world's oil and gas reserves occur in the sedimentary rocks, sandstones and carbonates, (see e.g. Boggs (2006)), we are especially interested in these rocks.

We will start by discussing sedimentary rocks. In this discussion we will especially emphasize the origin and internal structure of sandstones. The theory and illustrations are based upon Marshak (2001), Pettersen (1990), Boggs (2006), Gueguen and Palaciauskas (1994), Nesse (2000). Basically, the theory is similar for carbonates. However, the carbonate minerals are generally more susceptible to dissolution and less stable than most of the minerals present in sandstones. The mineralogy will therefore often change during the formation of carbonate rocks. For detailed information about origin, internal structure and composition of both sandstones and carbonates see Boggs (2006).

At the end of the chapter, we will relate the electric conductivity to pore fluid, composition, and internal structure of the rock. The discussion concerning the electric conductivity of a reservoir rock is mainly based upon the books of Gueguen and Palaciauskas (1994) and Mavko et al. (1998).

3.1 The Foundation of Rocks: Minerals

Let us start by shortly describing minerals which are the foundation of rocks. Every rock is composed of minerals. The most abundant group of minerals in the earth's crust is the silicate minerals. To define a mineral uniquely, both the chemical and molecular structure have to be specified. Because each

mineral possesses a specific chemical composition and molecular structure, it exhibits a distinct set of physical properties. These properties characterize how the mineral will respond to external disturbances like electric and magnetic fields. Since minerals are the foundation of a rock, physical, chemical and geometric properties of a rock depends on physical, chemical and geometric properties of the individual minerals, their volume fraction, and their distribution. The term microstructure is used to denote this complex internal geometry of a rock.

3.2 Sedimentary Rocks

Approximately 3/4 of the continental surface and almost the totality of the ocean floor is covered by sedimentary rocks. Since sandstones act as reservoir rocks for more than half of the world's gas and oil reserves, it is a very important sedimentary rock economically. The mineral composition of sandstones mainly consists of silicate grains like quartz and feldspars, ranging in size from 1/16-2 mm. We say that these grains constitute the framework fraction of the sandstone. On an average quartz, which possesses a superior hardness and chemical stability, makes up for 50-60 per cent of the framework fraction of sandstones. Another 10-20 per cent is made up of feldspars. Feldspars are chemically less stable than quartz and therefore more susceptible to chemical destruction during weathering and lithification.

We will now shortly describe the origin of sedimentary rocks. Sedimentary rocks descend from weathering of pre-existing rocks. The weathered products are transported by air or water to the spot of deposition and lithification. For information about weathering processes, weathering products, sediment transport, and depositional environments, see Boggs (2006) and Marshak (2001).

Lithification refers to the transformation of loose sediment into solid rock. The transformation first requires burial of the sediment. As a result of the burial, temperature and pressure will increase. With great burial, the pressure caused by the overburden forces sediment grains into closer contact and squeezes out trapped fluids, like water and air. We call this process compaction. The burial depths may reach tens of kilometres, and minerals which were stable at surface conditions, may during burial and compaction transform into other minerals. The compacted sediment will further be bound together when minerals like quartz and calcite precipitate from groundwater, filling open spaces, and attaching neighbouring grains. This step is the last step of lithification and geologists refer to this process as cementation.

3.2.1 Grain Orientation and Packing of Sedimentary Rocks

The fabric of sedimentary rocks is a function of grain orientation and packing. While grain packing refers to the spacing and density patterns of the grains, grain orientation tells us their orientation. Both grain orientation and packing are functions of size, shape, and degree of compaction of the sediment, and they control physical properties of the sedimentary rock. Some examples are density and porosity, which will be discussed in the following sections, and permeability, which will be discussed in the next chapter.

3.2.2 Porosity

Practically all materials in nature are porous. A porous material is composed of solid material and empty space, called pores. The bulk volume, V_B, is the total volume of the rock, i.e. the sum of the volume of the solid material, V_S, and the pore volume, V_P,

$$V_B = V_S + V_P \ . \tag{3.1}$$

The porosity, ϕ, of a material refers to the percentage of empty space in the material, and is given by

$$\phi = \frac{V_P}{V_B} \ . \tag{3.2}$$

Porosity therefore determines the volume of fluids that can be held in a particular reservoir rock.

The pore space may be generated during the sediment accumulation or after lithification. When the sediments accumulates, the grains do not perfectly fit together and empty space remains in between them. The porosity of an unlithified sediment depends on size, shape and sorting of the grains. For example, the porosity of a poorly sorted sediment, which is a mixture of grains of different size, is less than that of a well sorted sediment. The reason is that the smaller grains fill empty spaces between larger grains in a poorly sorted sediment. This is visualized in Figure 3.1.

After burial of the sediment during lithification, the weight of the overlying sediment forces the sediment grains into closer contact. The porosity of a sediment therefore tends to decrease with greater burial depth. We say we have compaction of the sediments. A sandstone having an original porosity of about 40 per cent, may during burial reduce its porosity to less than 10 per cent. The porosity of the compacted sediment may further decrease as a result of cementation. Minerals precipitate from groundwater and fill some

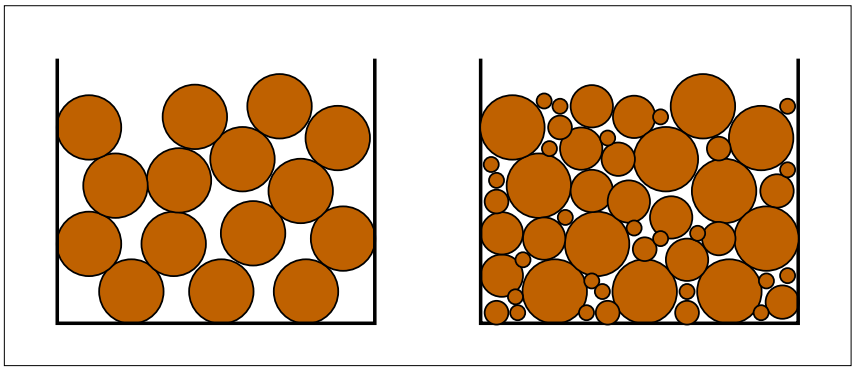

Figure 3.1: Illustration of a well sorted sediment to the left and a poorly sorted sediment to the right. Observe that the well sorted sediment has the highest porosity. Note that spherical grains are used only for simplicity.

of the pores. Nevertheless, a significant amount of porosity generally remains after lithification.

The changes in porosity after lithification are either due to fracturing of the sedimentary rock or dissolution of minerals. When rocks fracture, the opposing walls of the fracture do not fit together tightly, so a narrow space remains in between. Thus joints and faults may provide openings for fluids. Furthermore, if water passes through the rock, it may dissolve and remove minerals, resulting in an open space where it once was solid rock. Since the carbonate rock limestone is a soluble rock, caves due to dissolution of carbonate minerals are common.

3.2.3 Effective Porosity

If solid rock surrounds a pore completely, the fluid in the pore cannot flow to another location. Pores must therefore be linked for the fluids to flow. Since we are interested in extracting a fluid from a host rock, it is the connected pore system of the rock which is of further significance. The volume of this pore system is thus called the effective pore volume, V_E. It is this part of the pore system which is related to any flow in the material. Isolated pores and dead ends, illustrated in Figure 3.2, will not make a contribution to the effective pore volume. The effective porosity is defined by

$$\phi_{eff} = \frac{V_E}{V_B}. \tag{3.3}$$

It is the effective porosity which will be of further significance, and from now on, we use ϕ for effective porosity.

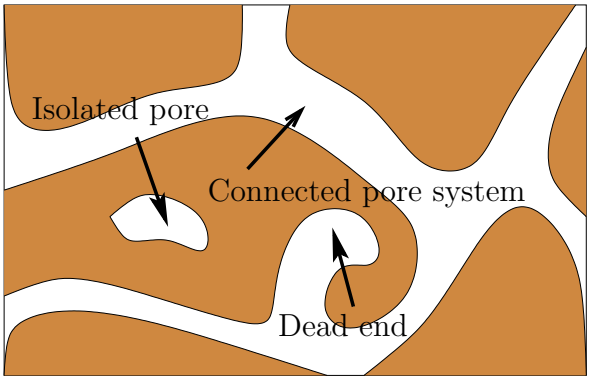

Figure 3.2: A micro scale pore system in which dead ends and isolated pores are illustrated.

3.3 Electric Conductivity of Porous Rocks

In Chapter 2 we learned that when a material is exerted to an electromagnetic field, the conductivity highly affects the response of the material. We will now consider porous rocks exerted to electromagnetic fields. In this thesis we assume that we have a flow of two fluids, namely oil and water. The reservoir rock thus comprises several mineral components and fluids, all affecting the conductivity of the material.

3.3.1 Porous Rocks Saturated with Fluids

Certain rocks containing high concentration of conductive minerals such as sulphides, magnetite, graphite, pyrite, and carbon may display high conductivity values. However, most crustal rocks consist of low-conductivity minerals, like silicates. As discussed above, one example is the major reservoir rock, sandstone. As a result of the low conductivity of the minerals, presence of fluids with high conductivity in the rock may increase the conductivity of the rock significantly.

The conductivity of saline water is approximately ten orders of magnitude larger than the conductivity of silicate minerals. This often makes the differences in conductivity between mineral grains comprising the rock very small, compared to the differences in conductivity between minerals and saline water. For instance, the conductivity of silicate minerals is of order $\sigma \approx 10^{-14}$- $\sigma \approx 10^{-10}$ S/m, while the conductivity of saline solutions lies in the range $\sigma \approx 10^{-1}$- $\sigma \approx 1$ S/m. It is therefore not surprising that even the modest amounts of water in porous silicate rocks can increase their

conductivity dramatically.

Effective Electric Conductivity and the Formation Factor

The effective electric conductivity, σ_{eff}, of a porous rock depends on the microstructure of the material. Consider a porous rock saturated with saline water, and recall the conductivity values for silicate minerals and saline water. As a result of the great conductivity differences, the electric currents will flow almost totally through the saline pore water. The microstructure of the pores thus indicates the path of the electric currents. Dead ends and isolated pores, illustrated by Figure 3.2, do not contribute to the effective conductivity.

Generally, the effective conductivity of a fully saturated rock is given by

$$\sigma_{eff} \equiv \frac{\sigma_w}{F} \,, \tag{3.4}$$

where σ_w represents the conductivity of the pore fluid and the factor F is called the formation factor. It depends on the microstructure of the rock, and the ratio between the conductivity of the solid, σ_s, and the conductivity of the pore fluid.

Since the electric conductivity of saline water is much larger than that of silicate minerals, the ratio σ_s/σ_w is essential zero when a porous rock is completely filled with saline water. The formation factor is then only dependent of the microstructure of the rock. If the porosity approaches one, $\phi \to 1$, the formation factor will approach one, $F \to 1$. This means that when the porosity approaches one, the effective conductivity will approach the conductivity of water, $\lim_{\phi \to 1} \sigma_{eff} = \sigma_w$. On the other hand, if the porosity approaches zero, $\phi \to 0$, the formation factor will approach σ_w/σ_s. According to equation (3.4), this means that when the porosity approaches zero, the effective conductivity will approach the conductivity of the solid, $\lim_{\phi \to 0} \sigma_{eff} = \sigma_s$.

Archie's Law

In the absence of detailed information about the pore microstructure, one must rely on empirical relations between the formation factor and the porosity to find the effective conductivity. Archie's law relates the porosity and formation factor for a rock completely filled with water. It is given by

$$F = (\phi - \phi_0)^{-m} \,. \tag{3.5}$$

Here m is approximately constant for a given rock type, ϕ is the porosity and ϕ_0 is the percolating porosity. The percolating porosity is a lower threshold

for conduction. Below this threshold, there is no conducting pathways, only isolated pores and dead ends. For most sedimentary rocks m is found to be in the range of $1.3 \leq m \leq 2.5$, with the majority of sandstone being close to $m = 2$. Carbonates, however, show a much wider range of variation and have m values as high as 5. The minimum value of m is 1, then the porosity is 1 and the rock is fully saturated with saline water. This corresponds to an open fracture.

In comparison with saline water, hydrocarbons possess a very low electric conductivity. Presence of oil instead of saline water in a reservoir rock will, therefore, dramatically reduce the effective electric conductivity of the rock. When both oil and water are present in a porous rock, the amount of each fluid is described by their saturations S_o and S_w. Saturations and flow of two fluids will be described more in details in the next chapter.

Archie's second law takes into account the presence of other fluids in addition to water. It relates the effective conductivity of a partially saturated rock to the saturation of saline water and the porosity by

$$\sigma_{eff} = (S_w^n \phi^m)\sigma_w \ . \tag{3.6}$$

Here the saturation exponent n is derived empirically. The value of n depends on the type of pore fluid and is different for gas-water saturations versus oil-water saturations. Normally n is around two, $n \approx 2$. However, the saturation exponents are experimentally found to be considerably larger when oil is the wetting fluid than if water is the wetting fluid. If oil is the wetting fluid, n lies in the range 2-9.5. We will describe wetting characteristics of fluids in the next chapter.

The empirical relationships described by Archie's laws are of particular importance in the petroleum industry. The conductivity measurements serve as one of the principle methods for estimating fluid saturations in oil-bearing rocks. In our study, we consider a known oil reservoir under water-assisted production. Due to the relation between fluid saturation and electric conductivity, monitoring of the front between oil and water by CSEM investigations which is repeated in time seems promising.

(Gueguen and Palaciauskas 1994)

Chapter 4

Reservoir Mechanics

As mentioned in the introduction, we will in this chapter discuss flow of fluids in a porous rock. We will start by discussing flow of one fluid in order to expand the theory to count for two fluids afterwards. For flow of one fluid, the modelling equations consider are Darcy's law, the mass conservation equation, the equation of state, and the equation of viscosity. The derivation of the conservation equation will not be included here. For the derivation of the conservation equation, see Pettersen (1990).

In order to describe the flow of two fluids in a porous rock, we have to describe the interactions in between them. Concepts like saturation, relative permeability and wetting properties will therefore be discussed. Then we will use this to expand the modelling equations to count for flow of two fluids. The theory and illustrations in this chapter are mainly based upon the books of Pettersen (1990), Gueguen and Palaciauskas (1994), and Marshak (2001).

4.1 Basic Concepts

The possibility for a fluid to pass through a porous material depends on the amount of connected pores as mentioned in Chapter 3. These pores are however tiny. Typically pore diameters are about 0.1 mm, and as a result, the friction between the flowing fluid and the solid material will be of great importance. Even though flow in larger channels, like in larger caves or in the wells, is described by common hydrodynamic laws, we will only consider the equations for flow in porous medium in this thesis. For information about flow in larger channels, see Kundu and Cohen (2004).

4.1.1 Permeability

Permeability describes the ability of a material to transmit fluids. The permeability depends on the size, straightness and number pores in the sedimentary rock. For instance, more fluid may pass through a rock with wider pores than narrow ones. Additionally, the flow is more rapid through straight pores than through crooked ones. If the pores are crooked, the distance a fluid molecule actually travels is many times the distance of the straight line between two end points. Notice that large porosity do not necessarily imply high permeability. A material whose pores are isolated from each other may have high porosity but low permeability.

Inhomogeneous and Anisotropic Material

In its general form, the permeability depends on both the direction of flow and the position in the material. Such a material is said to be inhomogeneous and anisotropic. The permeability tensor, $\boldsymbol{K}$, for a inhomogeneous and anisotropic material is given by

$$\boldsymbol{K} = \{k_{ij}(\boldsymbol{x})\}_{i=x,y,z;\ j=x,y,z} \ .$$

Homogeneous and Isotropic Material

If the permeability is independent of direction and position, the material is homogeneous and isotropic. The permeability tensor for a homogeneous and isotropic material is given by

$$\boldsymbol{K} = \{k_{ij} = k\}_{i=x,y,z;\ j=x,y,z} \ .$$

Inhomogeneous and Isotropic Material

When the permeability is independent of direction, but depends on the position, the material is said to be inhomogeneous and isotropic. The permeability tensor for an inhomogeneous and isotropic material is given by

$$\boldsymbol{K} = \{k_{ij}(\boldsymbol{x}) = k(\boldsymbol{x})\}_{i=x,y,z;\ j=x,y,z} \ .$$

Homogeneous and Anisotropic Material

For a homogeneous and anisotropic material, the permeability depends on the direction but is independent of the position. The permeability tensor for a homogeneous and anisotropic material is therefore given by,

$$\boldsymbol{K} = \{k_{ij}\}_{i=x,y,z;\ j=x,y,z} \ .$$

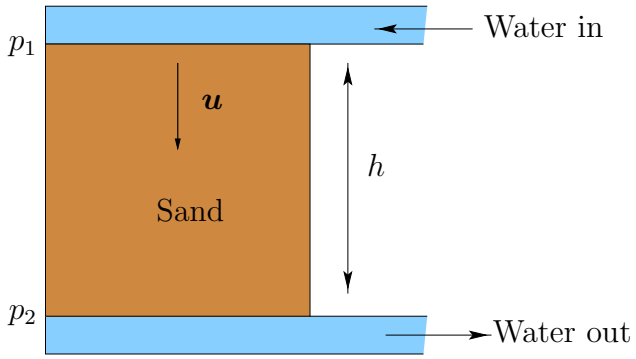

Figure 4.1: Schematically setup for Darcy's experiments.

4.1.2 Darcy's Law

In the middle of the 1850s the French engineer Henry Darcy performed several experiments with flow of water through different sand types. His experiments are illustrated by Figure 4.1. In every experiment the flow is vertically directed, and it passes through a sample of sand of height h. The average velocity, $\boldsymbol{u}$, of the water and the pressure p_1 and p_2 at the top and the bottom of the sample respectively, was measured. Regardless of the sand type, he found that the average velocity, $\boldsymbol{u}$, also called the Darcy velocity, was given by

$$\boldsymbol{u} = \alpha \frac{\Delta p}{h} \ , \tag{4.1}$$

where $\Delta p = p_1 - p_2$ is the pressure difference between the top and bottom of the sample, and α is a constant varying with the type of sand. Note that the Darcy velocity is an average velocity and not the pore velocity.

Darcy did only consider flow of water in his experiments. However, Darcy's law may be generalized for flow of any fluid. To take the variation of different fluids into account, we introduce the term viscosity, μ. The viscosity is a measure of the ability of a fluid to resist flow. A fluid with high viscosity thus flows hardly, while a fluid with low viscosity flows easily (see e.g. Boggs (2006)). If we further replace the constant α by the permeability tensor divided by the fluid viscosity, $\frac{\boldsymbol{K}}{\mu}$, and account for gravity, g, Darcy's law can be written,

$$\boldsymbol{u} = -\frac{\boldsymbol{K}}{\mu}(\nabla p + \rho g \boldsymbol{k}) \ , \tag{4.2}$$

where ρ is the fluid density. This is differential form of Darcy's law for one phase flow.

4.1.3 Conservation Laws

Conservation laws describe how a physical quantity, Γ, is preserved within a closed system. This means that the accumulation of Γ must be balanced by fluid flux and source or sink. From Pettersen (1990), the general conservation equation is

$$\frac{\partial \Gamma}{\partial t} + \nabla \cdot \Omega = Q \ .$$

Here Ω is the flux of the physical quantity, Γ, and Q is the source or sink term. The term, $\frac{\partial \Gamma}{\partial t}$, describes accumulation of Γ and $\nabla \cdot \Omega$ is the momentary difference of flux in and out of the closed system.

If the physical quantity is mass, $\phi\rho$, we obtain the mass conservation equation. Then the flux of mass is $\rho \boldsymbol{u}$. Assuming constant porosity, ϕ, the mass conservation equation becomes

$$\phi \frac{\partial \rho}{\partial t} + \nabla \cdot (\rho \boldsymbol{u}) = Q \ . \tag{4.3}$$

Considering a reservoir under production, production and injection wells in a reservoir represents sink and source respectively.

4.1.4 Equations of State

The relation, $\rho = \rho(p, T)$, between fluid density, temperature, and pressure is called an equation of state. For isothermal processes, i.e. processes with constant temperature, the equation of state is

$$\rho = \rho(p) \ . \tag{4.4}$$

Some of the most common equations of state are based on the definition of compressibility.

Compressibility and Incompressibility

The compressibility, c, is defined by:

$$c = -\frac{1}{V}\frac{dV}{dp} = \frac{1}{\rho}\frac{d\rho}{dp} \ , \tag{4.5}$$

where V is the volume of the fluid. The compressibility describes how much the volume of the fluid changes in response to squashing. For an incompressible fluid the density remains constant such that $\rho = \rho_0$ which implies that the compressibility equals zero.

4.1.5 Viscosity

Fluid viscosity, μ, is as mentioned earlier, a measure of the ability of a fluid to flow. Like density, viscosity vary as a function of temperature and pressure, $\mu = \mu(p, T)$. Since we will be considering isothermal processes only, the relation is given by

$$\mu = \mu(p) \ . \tag{4.6}$$

We have now got six equations (4.1)-(4.6) for the six unknowns $\boldsymbol{u}$, p, ρ, and μ. Hence the system of equations is closed. We will, however, need initial values and boundary conditions to solve the problem. For more information about initial values and boundary conditions, see Pettersen (1990).

4.2 Two Phase Flow

When several miscible fluids are present, we call each of them a phase. Each phase will occupy individual parts of the pore system. To describe flow of each phase separately, we have to describe their interaction. The complexity of a two phase problem is therefore larger than a one-phase problem, and more relations are needed to obtain a closed set of equations. We will now discuss flow of the two phases oil and water in porous rocks.

4.2.1 Saturation

When the two phases, oil and water, are present in a porous medium, the saturation, S_j, of each phase, $j = o, w$, is defined by

$$S_j = \frac{V_j}{V} \ . \tag{4.7}$$

Here V_j is the volume of phase in one volume unit, and V is the total effective pore volume in the volume unit. The sum of all the saturations is always one, $S_o + S_w = 1$.

4.2.2 Relative Permeability

Each phase will occupy some pore space. This yields a reduction in the permeability due to the presence of other phases. We thus introduce relative permeability, $k_{rj} = k_r(S_j)$, which depends on the saturation. The relative permeability is measured in the laboratory, and it will always be a number

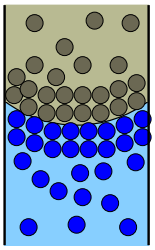

Figure 4.2: Illustration of the boundary between two fluids. Notice how the molecules are forced together near the boundary.

between zero and one. It is observed that the total permeability, $\boldsymbol{K}$, is reduced when there is a flow of several phases. This means that

$$k_{rj}(S_w) + k_{rj}(S_o) < 1 \,, \tag{4.8}$$

for any saturation.

4.2.3 Surface Tension and Capillary Pressure

When two fluids with different properties are in contact, forces will act between them. The molecules in each phase are forced closer together at the boundary by surface tension, $\boldsymbol{\psi}$. Thus as illustrated in Figure 4.2, the molecules here lie more tightly together than if we move away from the boundary. The surface tension, $\boldsymbol{\psi}$, between the phases are balanced by a pressure difference also called the capillary pressure, P_c. The capillary pressure is defined by

$$P_c = p_i - p_f = \frac{2\boldsymbol{\psi}}{r_m} \,, \tag{4.9}$$

where i and f denotes the phases, and r_m is the curvature radius, illustrated in Figure 4.3. From equation (4.9), we observe that the capillary pressure decreases with increasing curvature radius. The smallest pores in a porous media will thus be most highly affected by the capillary pressure, and small values of P_c is sufficient for flow in these pores. When the capillary pressure increases, larger pores are filled, and the amount of fluid in the porous material increases. As an example, consider Figure 4.4.

In equilibrium surface tension and capillary pressure will shape the boundary parting the phases. If the boundary is curved, the pressure always is largest on the concave side. This is illustrated in Figure 4.5.

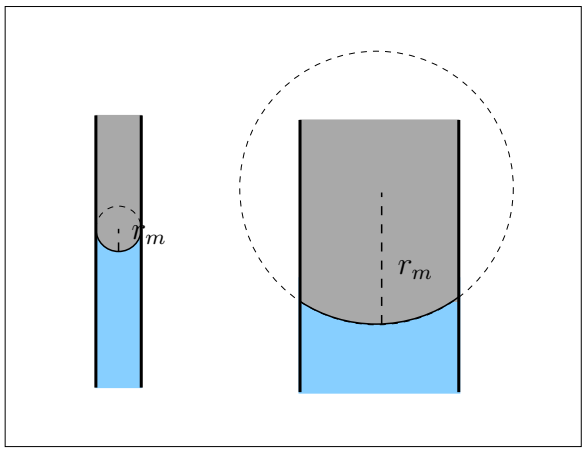

Figure 4.3: The curvature radius, r_m, on the boundary between two phases. Note that the curvature radius increase with increasing radius of the pipes.

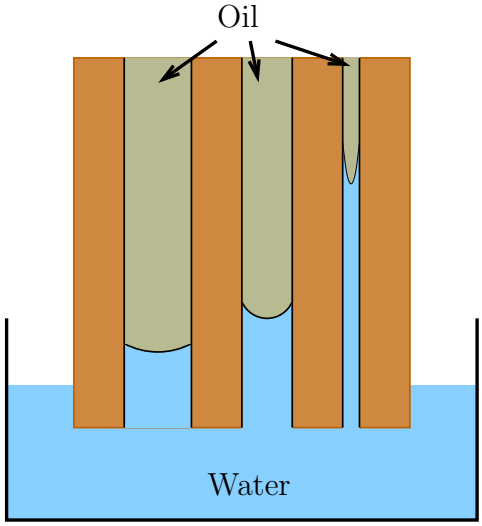

Figure 4.4: Visualization of an oil filled porous sample which is placed in water. Capillary pressure generates a flow of water into the sample. The pressure is largest in the narrow pores, and thus the water is highest here.

Wetting and non-wetting phase

Wetting properties of fluids determine which fluid that has the highest tendency to agglutinate the pore walls. Relative water, oil may be both the wetting and the non-wetting phase. However, in most of the reservoirs in the North Sea, water is the wetting phase or we have mixed wetting properties.

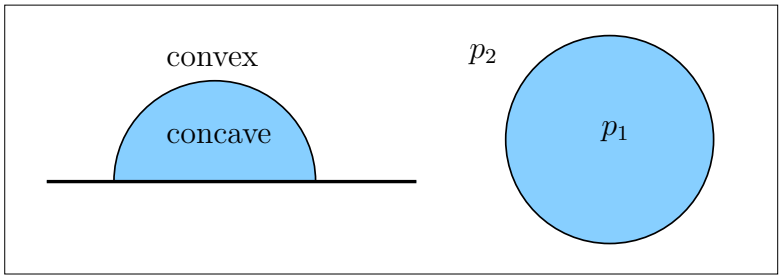

Figure 4.5: Illustration of the boundary between two phases. The pressure is always largest on the concave side, and hence, $p_1 < p_2$ in this case.

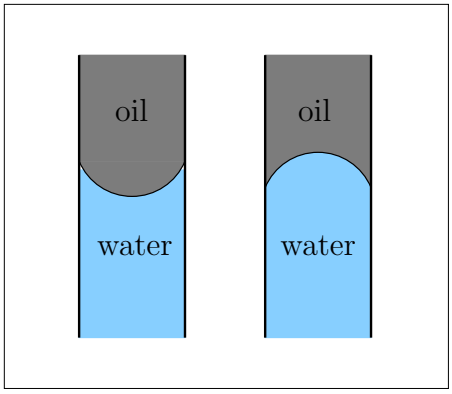

Figure 4.6: Illustration of the boundary between oil and water in glass pipes. Observe the various wetting properties. In the left-hand plot the wetting phase is water while the wetting phase in the right-hand plot is oil.

Lets us consider Figure 4.6. Observe the various wetting properties of oil and water in the two different pipes. In the left plot, water is the wetting phase, and oil is the wetting phase in the right plot.

Drainage and Imbibition

When a fluid is injected to displace another fluid, the distribution of the two fluids depends on their wetting properties. If the invading fluid is the wetting fluid, the process is called imbibition, while the process is called drainage if the invading fluid is the non-wetting fluid. For imbibition the invading fluid will first fill the smallest pores, while for drainage the invading fluid will first fill the largest pores. Capillary forces control the invasion. For more details, see Pettersen (1990) or Gueguen and Palaciauskas (1994).

4.2.4 Modelling Equations for Two Phase Flow

As mentioned earlier, to describe the flow of the phases separately, we have to describe their interaction. In the previous sections we have learned about the behaviour of the flow of two phases in porous media. In addition to the model equations (4.1)-(4.6) for each phase, we need to describe the interactions of the phases. The interaction between the phases is described by the saturations and the capillary pressure. Modelling equations for two phase flow are:
Darcy's law:

$$\boldsymbol{u}_j = -\boldsymbol{K}\frac{k_{rj}}{\mu_i}(\nabla p_j + \rho_j g\boldsymbol{k}) \tag{4.10}$$

Conservation of mass:

$$\nabla \cdot (\rho_j \boldsymbol{u}_j) + \phi\frac{\partial \rho_j S_j}{\partial t} = 0 \tag{4.11}$$

Equation of state:

$$\rho_j = \rho_j(p_j) \tag{4.12}$$

Viscosity:

$$\mu_j = \mu_j(p_j) \tag{4.13}$$

Saturation:

$$S_w + S_o = 1 \tag{4.14}$$

Capillary pressure:

$$p_o - p_w = P_c(S_w)\ . \tag{4.15}$$

The unknowns are $\boldsymbol{u}_j$, p_j, ρ_j, μ_j, and S_j, for each phase, $j = o, w$. This makes totally 14 unknowns and 14 equation. The system of equations is then said to be closed, but as for flow of one phase, we need boundary values and initial values to solve the problem.

The theory and equations described in this chapter constitute a fundamental basis for simulation of fluid flow in a reservoir. Only flow of two phases are discussed, but the theory may be expanded to flow of several phases.

Chapter 5

Controlled Source Electromagnetic Monitoring

In this chapter we will start by considering the use of marine controlled source electromagnetic (CSEM) data for reservoir production monitoring. The model setup for the numerical computations will be presented, and we will discuss the various types of noise that will cause errors in the electromagnetic data. The discussion and illustrations are mainly based upon the paper of Lien and Mannseth (2008) and Flosadottir and Constable (1996). At the end of the chapter errors caused by an erroneous representation of the location and orientation of the receivers will be discussed.

5.1 Electromagnetic data for Investigation of the Marine Subsurface

If we consider Maxwell's equations (2.24)-(2.27) in integral form derived in Chapter 2, we see that the anomalous electric and magnetic fields depend on the complex electric conductivity of the anomaly. For this reason electromagnetic waves are used to detect objects of anomalous conductivity in the subsurface. Since the frequency used in this study is low, we will from now on neglect the term $i\omega\varepsilon$ in equation 2.11 and write $\tilde{\sigma} = \sigma$. We recall from Chapter 3 that the electric conductivity of a porous rock is strongly influenced by the fluid saturations in the pores. For instance, the conductivity of a porous rock saturated with hydrocarbons will lie in the range 0.002-0.033 S/m, while the corresponding range for a porous rock saturated with saline water will be 0.50-2.00 S/m (see e.g. Lien and Mannseth (2007)). This major difference in conductivity was utilized when a methodology for detection of hydrocarbon reservoirs in deep-water areas was developed (see e.g.

Eidesmo et al. (2002)).

It has several times been proposed that CSEM may be used to detect changes in a reservoir over a period of time (see e.g. Eidesmo et al. (2004), Ellingsrud et al. (2005), and Eidesmo et al. (2006)). If we are considering a reservoir under water-assisted production, the conductivity distribution in the reservoir will change as a result of incoming saline water and the front that separates the fluids will develop. We will now discuss the use of CSEM data for monitoring of a reservoir under water-assisted production.

Previous investigations that involve electromagnetic data for production monitoring have considered cross-borehole induction (see e.g. Malinverno and Torres-Verdin (2000), Wilt and Morea (2004)). The reservoirs of interest are generally about 1 km or more below the sea floor (see e.g. Eidesmo et al. (2004), Ellingsrud et al. (2004), Ellingsrud et al. (2005), and Ellingsrud et al. (2006)). In order to obtain a desirable resolution of the data in an electromagnetic survey, short wavelengths and correspondingly high frequencies are necessary. However, short wave lengths suffer from very high attenuation. In order to reach the potential target with electromagnetic waves, we have to use longer wavelengths, and lower frequencies. The frequency may be within a decade of 0.1 Hz, and the wavelength is in order of kilometres (see e.g. Lien and Mannseth (2008)). Unfortunately, long wavelengths and low frequencies do not provide the sufficient resolution. This means that it may be difficult to obtain a high resolution while inverting for electric conductivity.

In comparison with exploration, monitoring of the flooding front is even more challenging with respect to resolution. This is because the aim is to identify local changes in the structure of conductivity distribution during flooding, and the signals from the flooding front is expected to be weaker than for exploration setting. It is therefore important to assess the attainable resolution from 4D EM data both alone and in combination with other data types, like 4D seismic data. Nevertheless, we will in this work only be studying the attainable resolution from 4D EM data alone. We will therefore investigate the ability of the electromagnetic signals to overcome realistic noise.

The monitoring process does, however, offer some advantages compared to exploration. Firstly, the existence and location of the reservoir are already established prior to the monitoring. For this reason, the identification may be based on a reasonably good initial description of the conductivity distribution of the subsurface and the location of the reservoir. Secondly, the same equipment may be applied for successive acquisitions, and thus the initial implementation of new equipment for a given target will make up the main cost of CSEM instrumentation. Continuous monitoring of a fixed target will therefore yield good values for these investments, and extensive

instrumentation may be applied in long-term monitoring of a hydrocarbon reservoir. Thirdly, since the the acquisitions will be repeated in time, some of the errors may partially cancel in the time-lapse signal that will be defined in Section 5.3.

5.2 Modelling Equations

In Chapter 2 we denoted the components of the electric field and magnetic field E_j and H_j for $j = x, y, z$. The expression $\boldsymbol{F}$ will now be used as a common notation for $\boldsymbol{E}$ and $\boldsymbol{H}$ where this is convenient. Similarly, we will use F_j to denote either E_j or H_j.

Since saline water is injected in the reservoir, the anomalous conductivity distribution will be a function of space and time: $\sigma^a = \sigma^a(\boldsymbol{r}, t)$. We assume the background conductivity distribution, σ^b, to be a function of space, $\sigma^b = \sigma^b(\boldsymbol{r})$, only. This gives us

$$\sigma(\boldsymbol{r}, t_i) = \sigma^b(\boldsymbol{r}) + \sigma^a(\boldsymbol{r}, t_i) \ , \tag{5.1}$$

where t_i denotes the time of acquisition number i. Correspondingly, the components of electromagnetic fields is given by

$$F_j(\boldsymbol{r}, t_i) = F_j^b(\boldsymbol{r}) + F_j^a(\boldsymbol{r}, t_i) \ . \tag{5.2}$$

Let us now recall Maxwell's equations from Chapter 2

$$\begin{aligned}
\boldsymbol{E}^b(\boldsymbol{r}') &= \iiint_\Omega \boldsymbol{G}_b^{\boldsymbol{E}}(\boldsymbol{r}'|\boldsymbol{r})\boldsymbol{j}^e(\boldsymbol{r})d\boldsymbol{r} \ , \\
\boldsymbol{H}^b(\boldsymbol{r}') &= \iiint_\Omega \boldsymbol{G}_b^{\boldsymbol{H}}(\boldsymbol{r}'|\boldsymbol{r})\boldsymbol{j}^e(\boldsymbol{r})d\boldsymbol{r} \ , \\
\boldsymbol{E}^a(\boldsymbol{r}') &= \iiint_\Gamma \boldsymbol{G}_b^{\boldsymbol{E}}(\boldsymbol{r}'|\boldsymbol{r})\sigma_a(\boldsymbol{r})(\boldsymbol{E}^a(\boldsymbol{r}) + \boldsymbol{E}^b(\boldsymbol{r}))d\boldsymbol{r} \ , \\
\boldsymbol{H}^a(\boldsymbol{r}') &= \iiint_\Gamma \boldsymbol{G}_b^{\boldsymbol{H}}(\boldsymbol{r}'|\boldsymbol{r})\sigma_a(\boldsymbol{r})(\boldsymbol{E}^a(\boldsymbol{r}) + \boldsymbol{E}^b(\boldsymbol{r}))d\boldsymbol{r} \ ,
\end{aligned}$$

where $\boldsymbol{r}'$ denotes a receiver position.

5.3 The Time-lapse Signal

In order to monitor the flooding front in a reservoir under water-assisted production, the acquisition is repeated in time. Thus we obtain information

about the 3D subsurface over time. Such a survey is therefore called a 4D EM survey. The time-lapse difference of F_j is defined by

$$\delta(F_j) = F_j(\boldsymbol{r}, t_{i+1}) - F_j(\boldsymbol{r}, t_i) \ , \tag{5.3}$$

where $F_j(\boldsymbol{r}, t_i)$ and $F_j(\boldsymbol{r}, t_{i+1})$ denotes an arbitrary electric or magnetic field component in two successive acquisitions. The first is taken at time $t = t_i$ and the second at time $t = t_{i+1}$. For simplicity we will from now on denote $F_j^{(i)} = F_j(\boldsymbol{r}, t_i)$ and $F_j^{(i+1)} = F_j(\boldsymbol{r}, t_{i+1})$. Usually, the magnitude of the time-lapse signal δF_j is much smaller than the magnitudes of $F_j^{(i)}$ or $F_j^{(i+1)}$. To avoid numerical cancellation of significant digits when forming δF_j, we need a relatively high accuracy in $F_j^{(i)}$ and $F_j^{(i+1)}$. This has been taken into account in the numerical calculations.

The electromagnetic field may be described by its amplitude, A, and phase, P. We let $\hat{g}$ denote amplitude and phase of the electromagnetic field components, F. The aim is to consider $\hat{g}$ at two points in time. The difference, called the time-lapse difference, is given by

$$\delta\hat{g}(F_j) = \hat{g}(F_j^{(i+1)}) - \hat{g}(F_j^{(i)}) \ , \tag{5.4}$$

where $\hat{g}(F_j^{(i)})$ and $\hat{g}(F_j^{(i+1)})$ are amplitude or phase of the electromagnetic field component, F_j, measured by a receiver at the times $t = i$ and $t = i + 1$ respectively.

5.4 The Model Setup

In this work we will be considering an anomaly which is embedded in a background. The anomaly refers to the region of the porous rock saturated with hydrocarbons, while the background refers to a porous rock saturated with saline water. The initial area of anomalous conductivity constitutes the reservoir. We will assume that the conductivity of the region of the reservoir which is filled with water has the same conductivity distribution as the background. See Figure 5.1.

When defining the experimental setup, there will be an optimal distance between the source, the receivers, and the object to be identified. If the receivers are too close to the source, the data will be dominated by the wave propagating directly through the highly conducting water towards the receivers. Furthermore, if the distance is too large, the air-wave will dominate the data. This is because electromagnetic waves travel more slowly inside a medium of high electric conductivity than in a medium of low electric conductivity (see e.g. Ellingsrud et al. (2004), Eidesmo et al. (2006)).

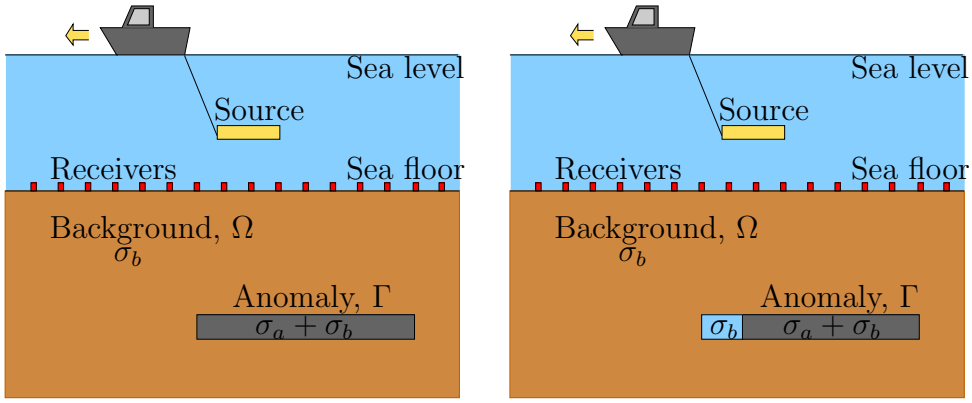

Figure 5.1: The experimental setup at time $t = t_0$ to the left and $t = t_1$ to the right. An electromagnetic source is towed behind a vessel generating electromagnetic waves that penetrates the marine subsurface before it is measured by the receivers. At time $t = t_1$, saline water has been injected. If we compare the two experimental set-ups, we will see that the area of anomalous conductivity distribution has changed.

In the monitoring process, the object to be identified is the water flooded region. The positioning of the source and receivers relative to the flooding front will therefore affect the quality of the signals. In order to obtain an optimal signal strength, Lien and Mannseth (2007) found an optimal location of a horizontal electric dipole (HED) source which is oriented along the x-axis. The investigation was performed with receivers located in a 1D grid at the sea-floor along the x-axis, and the optimal location was found to be about 1 km from the front along the negative x-axis.

In this study, the receivers will be located in a 2D grid 'at the sea-floor' 100 m apart. The experimental setup is illustrated in Figure 5.2 and Figure 5.3. As in the paper of Lien and Mannseth (2008), no simulation of fluid flow will be performed in the current work. Instead we have considered the response of the electromagnetic field to direct perturbations in the in the electric conductivity distribution. For convenience, we will nevertheless use terminology like 'during flooding' and so on, where this is natural. We will focus on changes in the electric conductivity caused by horizontal flooding only, and the horizontal shape of the transition zone parting the two phases is in this work assumed to be planar. This is illustrated in Figure 5.2. In principle, CSEM may also be applied to resolve vertical features of the front (see e.g. Malinverno and Torres-Verdin (2000), Wilt and Morea (2004)).

All numerical computations will be performed with a full integral solver

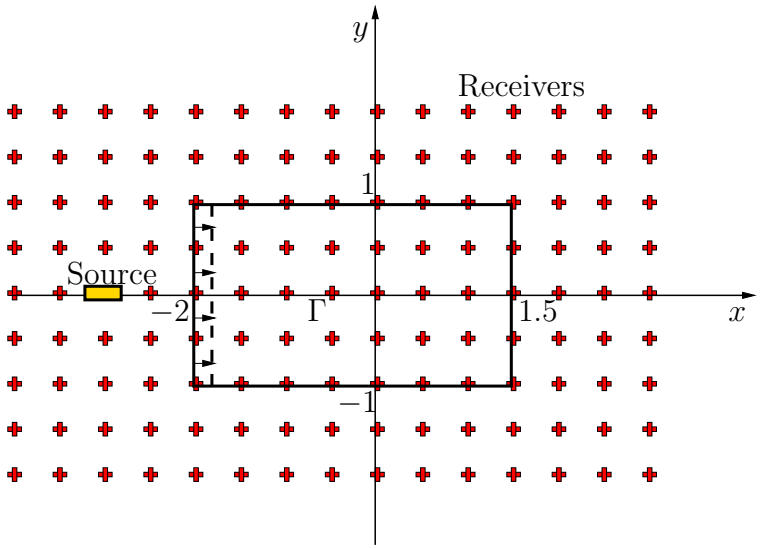

Figure 5.2: Illustration of the optimal location of the the source relative to the flooding front seen from above. Initially, the hydrocarbons cover the region $\Gamma(t_i) = \{\boldsymbol{r}|x \in [-2.0, 1.5], y \in [-1.0, 1.0], z \in [-1.1, -1]\}$, while $\Gamma(t_{i+1}) = \{\boldsymbol{r}|x \in [-1.8, 1.5], y \in [-1.0, 1.0], z \in [-1.1, -1]\}$. Note that the scale of the distance between the receivers is not correctly represented.

Table 5.1: Source parameters.

Current	**Dipole range**	**Frequency**
1000 A	100 m	0.1 Hz

Table 5.2: Conductivity distribution.

Ocean water	**Water-saturated rock**	**Oil-saturated rock**
3.33 S/m	1.00 S/m	0.01 S/m

(Hursan and Zhdanov 2002), (Zhdanov 2002). This solver uses analytic Green's tensors and is therefore applicable to horizontally layered background conductivity distributions. Table 5.1 and Table 5.2 gives the source parameters and the conductivity distribution respectively. This will be used in the electromagnetic forward modelling.

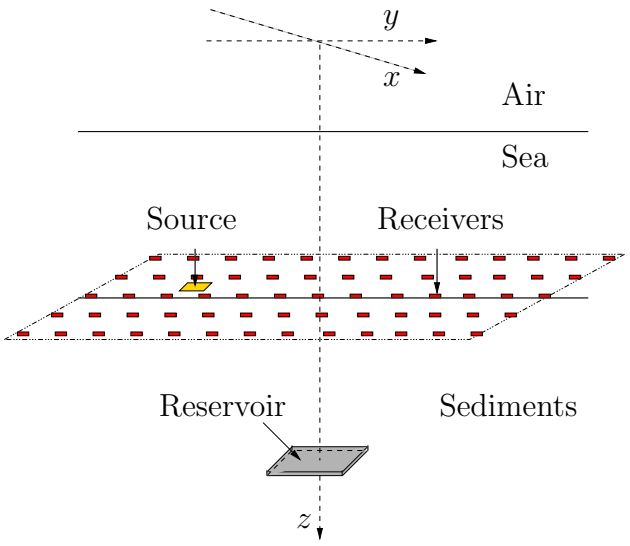

Figure 5.3: A sketch of the model setup. An oil-saturated reservoir is embedded water-saturated sediments 1000 m below the sea-floor below sea level. The sea-floor is horizontal, and the depth is constantly 1000 m. The receivers are placed in a 2D grid constantly at depth 998 m below sea level.

5.5 Errors in the CSEM Data

During the survey and the modelling of the data there will be several uncertainties. Due to these uncertainties, there will be errors in the measured electromagnetic field. The errors may either be measurement errors, $\epsilon_g^d(F_j)$, or modelling errors, $\epsilon_g^m(F_j)$. Let us briefly discuss both before continuing with the errors of special concern in this study.

5.5.1 Measurement Errors

Measurement errors, ϵ_g^d, are random in nature, and we often use a Gaussian distribution to model these errors. The instrumental noise level varies with frequency and antenna length. However, for a given frequency and antenna length the magnitude of the noise level is constant. This constant noise level defines a lower threshold for the strength of the signal.

In the paper of Webb et al. (1985) and Flosadottir and Constable (1996), the instrumental noise is taken to vary as f^{-1}, levelling out above 1 Hz. At frequencies within a decade or two of 1 Hz, the deep sea-floor is electrically a very quiet environment. This means that the instrumental noise will dominate the noise spectrum for these frequencies.

Furthermore, the instrumental noise is in Webb et al. (1985) and Flosadottir and Constable (1996) taken to produce a voltage independent of the receiver antenna length. Typically, the length of a receiver antenna is between 10 m for an electric field instrument and $200 - 3000$ m in long-wire electromagnetic instruments (Lien and Mannseth 2008). When the instrumental noise is interpreted as an electric field value, it will scale inversely with the antenna length. The sensitivity of the receiver may thus be increased by increasing the antenna length. This means that we will experience lower instrumental noise when the length of the antenna is increased.

Electromagnetic fields attenuate very rapidly with range. For this reason the magnitude of the instrumental noise is rarely comparable to the magnitude of the signal. For weak signals, ϵ_g^d will be dominated by instrumental noise. When the field is increased, errors depending on the magnitude of F comes into play. These errors are positively correlated with the field strength for all F. The degree of correlation is, however, weaker for larger values of F, and consequently the signal-to-noise ratio will be largest for large values of F

Reduction of measurement errors, ϵ_g^d, may be achieved by stacking the recorded data. Effective stacking will increase the signal-to-noise ratio by a factor of $\sqrt{N}$, where N is the number of stacking points within the stacking window (e.g. Lien and Mannseth (2008), Fowler (2005)). Since the evolution of the flooding front in a reservoir is extremely time consuming, multiple measurements can be executed rapidly. If we are considering towed sources, the number of data-points, N, in the stacking window depends on the travelling distance of the vessel during collection and the frequency of the transmitted field. If the travelling distance is large, each acquisition will be more time consuming. This means that within a given time, fewer acquisitions may be performed than for smaller travelling distances. Fixed sources may therefore enhance the quality of the data since the data points will be restricted by the propagating front only.

5.5.2 Modelling Errors

The electromagnetic fields may also consist of errors that are quite different from measurement errors. These errors are called modelling errors, ϵ_g^m, and they are caused by an incorrect representation of features in the mathematical model. Physical parameters that are not correctly represented in the model may cause systematic errors in the interpretation of the data, and the results may therefore be biased.

One example of modelling errors is ambient electronic noise. Ambient electronic noise is either due to telluric currents or ocean-induced fields. Tel-

luric currents are induced by changes in the outer part of earth's magnetic field, and they will on dry land exist on the entire frequency range. However, the receivers are placed at the sea-floor, and we know that saline water has a relatively high electric conductivity. The telluric noise will therefore be reduced with increasing water depths. At depths larger than a few hundred meters the magnitude of this type of ambient noise will be small for frequencies above 1 Hz. However, at lower frequencies, the telluric currents will first begin to contaminate the signal and then the ocean-induced fields begin to contaminate the signal. Ocean-induced fields are caused by interactions between ocean currents and earth's magnetic field. These currents may for example be ocean tides or intense currents like the Gulf Stream. Ocean-induced fields may, however, also be caused by surface gravity waves, microseism, swell, and wind waves that will produce fluctuations in velocity and pressure at the sea-floor. These fluctuations will in turn induce local electromagnetic fields which will be strongly dependent of local geology and the state of the sea.

In Flosadottir and Constable (1996) ambient noise is modelled to vary as f^{-2}, passing through a value of 10^{-10} V/(m$\sqrt{\text{Hz}}$) at 0.1 Hz. In order to reduce ambient noise the electromagnetic field may be measured prior to the subsurface investigation and independently of the controlled source. The results may then be taken into account when the fields that are induced by the controlled source are analysed.

Modelling errors may also be caused by an incorrect representation of the structures in the subsurface. The subsurface may consist of complex structures with fine-scale variations. If we do not possess adequate information about these structures and variations, we may incorrectly model the electric conductivity of the background sediments and the reservoir. For example, the conductivity values of the background may have been over-estimated, or objects of low conductivity, like salt or volcanic structures, may have been neglected. Presence of such systematic errors will cause the calculated field to be biased. The calculated field will thus be shifted in one direction if compared to the actual field values (Lien and Mannseth 2008).

Furthermore, the computer power is restricted, and an approximately, smoothly varying model of the subsurface is therefore often used. Both the lack of information and neglection of fine-scale variations in conductivity will originate modelling errors in the results. The modelling errors caused by neglecting fine-scale variations in the electric conductivity of the subsurface may be reduced by stacking measurements from receivers that are located closely in space (Lien and Mannseth 2008).

Uncertainties in the location and orientation of the source and receivers give us additional modelling errors. In exploration the source is towed behind

a vessel. The accuracy of the determination of position and orientation will thus depend on the physical conditions during the acquisition, and these conditions may vary from one acquisition to another.

A sensitivity study for production monitoring is presented by Lien and Mannseth (2008), in which the effect of modelling errors that are due to erroneous conductivity distribution is discussed. In this work, we will continue the sensitivity study of modelling errors presented by Lien and Mannseth (2007). Here modelling errors due to uncertainties in the location and orientation of source and receivers will be considered more closely. Let us first consider the errors due to uncertainties in the receiver.

5.6 Uncertainty in the Location and Orientation of the Receivers

The amplitude, $\hat{A}$, or phase, $\hat{P}$, of an electromagnetic field component computed for the reference location and orientation of the receivers is denoted $\hat{g}(F_j)$. The reference position and orientation may, however, be erroneously represented. The true amplitude, A, or phase, P, of an electromagnetic field component is given by

$$g(F_j) = \hat{g}(F_j) + \epsilon_g(F_j) \ , \tag{5.5}$$

where $\epsilon_g(F_j)$ is the errors in the true amplitude or the phase caused by the erroneous representation of the location or orientation of the receivers.

To be useful for monitoring, it is important that the signal, $\delta(g_{F_j})$, caused by the moving front exceeds the associated errors in the data. These associated errors, called the time-lapse errors, $\delta\epsilon_g(F_j)$, are given by

$$\delta\epsilon_g(F_j) = \epsilon_g(F_j^{(i+1)}) - \epsilon_g(F_j^{(i)}) \ , \tag{5.6}$$

where $\epsilon_g(F_j^{(i)})$ and $\epsilon_g(F_j^{(i+1)})$ are the errors of the amplitude or the phase of the electromagnetic field component, F_j, at the times $t = i$ and $t = i + 1$ respectively.

Some errors are time invariant or close to time invariant. If this is the case, a considerable cancellation of the errors from $\epsilon_g(F_j)$ to $\delta(\epsilon_g(F_j))$ is expected to take place. This entails that the errors will have small influence on the time-lapse signal, $\delta(\hat{g}_{F_j})$.

In this study, we have computed the electromagnetic fields for the reference location and orientation of the receivers and for the true location or orientation of the receivers. The numerical computation has been performed

before and after flooding of the reservoir for both cases. We have thus been able to find the reference time-lapse signal and the true time-lapse signal which both have been plotted for the 2-D grid of receivers. In Chapter 6 these results will be presented. In order to study the sensitivity of the signal, we want to compare $\delta\hat{g}(F_j)$ to $\delta g(F_j)$.

5.6.1 Uncertainty in the Location of the Receivers

As mentioned earlier, the receivers are placed 'at the sea floor'. We consider the reference locations of the receivers to be located 100 m apart in a 2-D grid that covers the region $R = \{\boldsymbol{x}|x \in [-3075, 9975], y \in [-9975, 9975]\}$. Unfortunately, the true location of the receivers may differ from the reference location. We will in this study assume the deviation from the reference location is maximum ± 10 m. In order to study the sensitivity of the data, we have performed several experiments with various perturbations. The various experiments will be further discussed in Chapter 6.

5.6.2 Uncertainty in the Orientation

When we are considering the orientation of the receivers, we are going to study the components of the electric field only. To be able to measure the electric field in three dimensions, the receivers are constructed like a coordinate system as shown in Figure 5.4. Imagine the reference coordinate

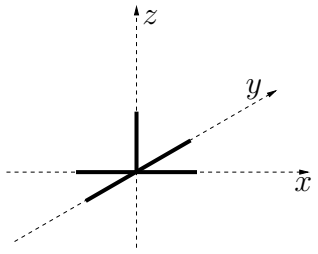

Figure 5.4: Illustration of the electromagnetic receiver. Notice that is consist of three orthogonal antennae in order to measure the three dimensional electromagnetic field..

system, (x, y, z), in which the x-axis is assumed to be parallel and the y-axis is assumed to be perpendicular to the electromagnetic dipole. They both lie at a horizontal sea-floor. The z-axis of the reference coordinate system is considered to be vertical.

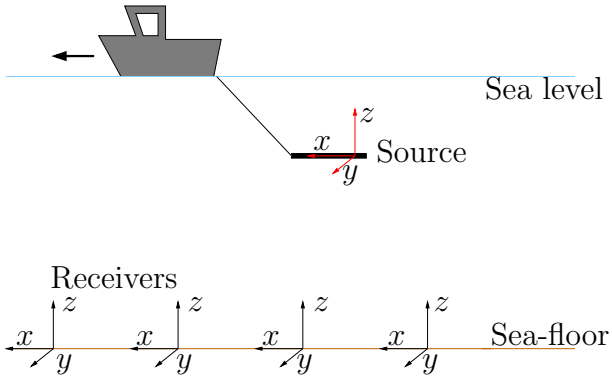

Figure 5.5: Notice how the orientation of the source is used to define the reference coordinate system, (x, y, z), for the receivers.

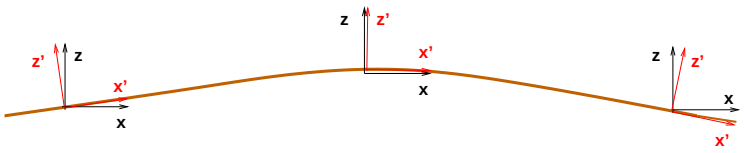

Figure 5.6: Illustration of the reference orientation, (x, z), and the true orientation, (x', z'), of the receivers. Notice the tilting of the true orientation caused by variations in the sea-floor.

In each acquisition, we expect the orientation of the receivers to coincide with the reference coordinate system. This is illustrated in Figure 5.5. However, when the receivers are placed at the sea-floor, there may be some uncertainties in their orientation. This uncertainty is due to either rotation or tilting of the receivers. Since the receivers do not necessarily completely coincide with the reference coordinate system, we will define a new coordinate system (x', y', z') which gives us the true orientation of the receivers. This true orientation will vary from one receiver to another.

For simplicity, we will consider uncertainties in the orientation of the receivers in two dimensions. Let us first consider the tilting case. Figure 5.6 shows the reference orientation, (x, z), and the true orientation, (x', z'), of three receivers. The electromagnetic forward modelling will give us the components of the electric field vector, $\boldsymbol{E}$. Since we expect the orientation

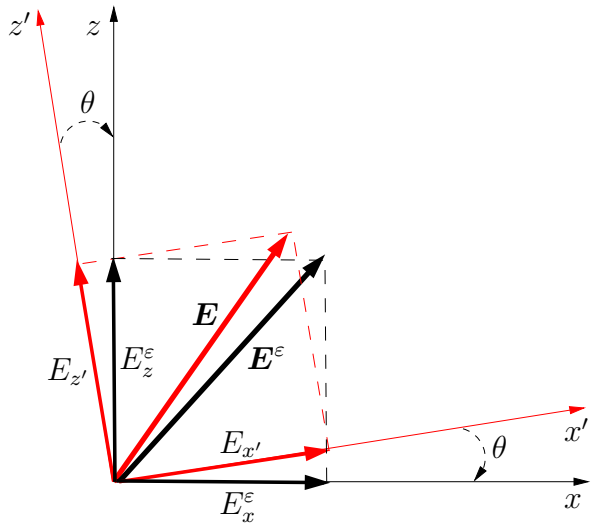

Figure 5.7: Illustration of the components of $\boldsymbol{E}^{\varepsilon}$ in black and $\boldsymbol{E}$ in red. Notice that $\boldsymbol{E}^{\varepsilon}$ and $\boldsymbol{E}$ do not coincide.

of the receivers to coincide with the reference coordinate system, (x, z), we will expect the components of the electric field vector to coincide with the reference coordinate system, (x, z). However, since the orientation may be tilted, the components that we are measuring are in reality $E_{x'}$ and $E_{z'}$. In Figure 5.7 the true orientation of one receiver is shown together with its reference orientation.

In order to investigate the sensitivity of the electromagnetic data, we want to compare $\boldsymbol{E}^{\varepsilon}$ to $\boldsymbol{E}$. The components, E_x^{ε} and E_z^{ε}, of $\boldsymbol{E}^{\varepsilon}$, are shown in Figure 5.7 while the components, E_x and E_z, of $\boldsymbol{E}$, are shown in Figure 5.8. In the forward modelling we will find the components, E_x^{ε} and E_z^{ε}, of $\boldsymbol{E}^{\varepsilon}$. In order to find the components, E_x and E_z, we want to transform $E_{x'}$ and $E_{z'}$ into the reference coordinate system, (x, z).

For convenience, we will now let $E_{x'} = v_x$ and $E_{z'} = v_z$. Each of them consists of a real part and an imaginary part such that $v_x = v_x^R + iv_x^I$ and $v_z = v_z^R + iv_z^I$. Represented in coordinate system (x', z'), the electric field vector, $\boldsymbol{E}$, is given by

$$\boldsymbol{E}_{(x',z')} = v_x \boldsymbol{e}'_x + v_z \boldsymbol{e}'_z = (v_x^R + iv_x^I)\boldsymbol{e}'_x + (v_z^R + iv_z^I)\boldsymbol{e}'_z \,, \tag{5.7}$$

where $\boldsymbol{e}'_x$ and $\boldsymbol{e}'_z$ are normal unit vectors of the coordinate system(x', z'), as illustrated in Figure 5.9. We divide equation 5.7 into one equation for the

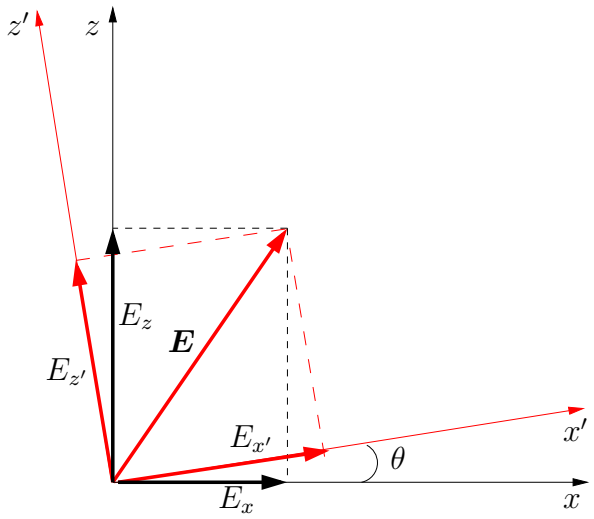

Figure 5.8: The components of $\boldsymbol{E}$ represented in both coordinate systems. The black axes illustrates the reference coordinate system(x, z) while the red axes illustrates the coordinate system(x', z').

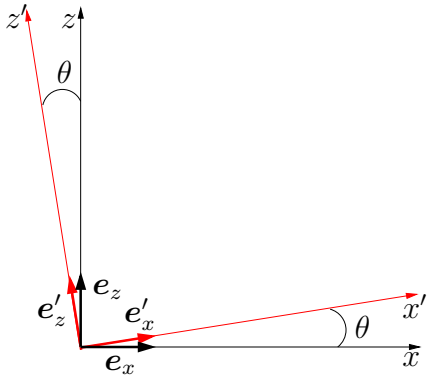

Figure 5.9: Illustration of the normal unit vectors $\boldsymbol{e}_x$ and $\boldsymbol{e}_z$ of the reference coordinate system, (x, z), and the normal unit vectors $\boldsymbol{e}'_x$ and $\boldsymbol{e}'_z$ of the coordinate system(x', z').

real part and one equation for the imaginary part

$$\boldsymbol{E}^R_{(x',z')} = v^R_x \boldsymbol{e}'_x + v^R_z \boldsymbol{e}'_z \,, \tag{5.8}$$

$$\boldsymbol{E}^I_{(x',z')} = v^I_x \boldsymbol{e}'_x + v^I_z \boldsymbol{e}'_z \,. \tag{5.9}$$

In order to represent the electric field vector in the reference coordinate

system, the normal unit vectors $\boldsymbol{e}'_x$ and $\boldsymbol{e}'_z$ are given by

$$\begin{aligned} \boldsymbol{e}'_x &= (\boldsymbol{e}'_x \cdot \boldsymbol{e}_x)\boldsymbol{e}_x + (\boldsymbol{e}'_x \cdot \boldsymbol{e}_z)\boldsymbol{e}_z \ , \\ \boldsymbol{e}'_z &= (\boldsymbol{e}'_z \cdot \boldsymbol{e}_z)\boldsymbol{e}_z + (\boldsymbol{e}'_z \cdot \boldsymbol{e}_x)\boldsymbol{e}_x \ . \end{aligned}$$

This gives us

$$\boldsymbol{e}'_x = \cos(\theta)\boldsymbol{e}_x + \cos(90-\theta)\boldsymbol{e}_z \ , \tag{5.10}$$
$$\boldsymbol{e}'_z = \cos(\theta)\boldsymbol{e}_z + \cos(90+\theta)\boldsymbol{e}_x \ . \tag{5.11}$$

By substituting this into equations (5.8) and (5.9), the electric field vector, $\boldsymbol{E}$, may be represented in the reference coordinate system

$$\begin{aligned} \boldsymbol{E}^R_{(x,z)} &= v^R_x(\cos(\theta)\boldsymbol{e}_x + \cos(90-\theta)\boldsymbol{e}_z) + v^R_z(\cos(\theta)\boldsymbol{e}_z + \cos(90+\theta)\boldsymbol{e}_x) \ , \\ \boldsymbol{E}^I_{(x,z)} &= v^I_x(\cos(\theta)\boldsymbol{e}_x + \cos(90-\theta)\boldsymbol{e}_z) + v^I_z(\cos(\theta)\boldsymbol{e}_z + \cos(90+\theta)\boldsymbol{e}_x) \ . \end{aligned}$$

This gives us:

$$E_x = (v^R_x\cos(\theta) + v^R_z\cos(90+\theta)) + (v^I_x\cos(\theta) + v^I_z\cos(90+\theta))i \ , \tag{5.12}$$
$$E_z = (v^R_x\cos(90-\theta) + v^R_z\cos(\theta)) + (v^I_x\cos(90-\theta) + v^I_z\cos(\theta))i \ . \tag{5.13}$$

In a similar manner, we may for rotation of the receivers find expressions for E_x and E_y:

$$E_x = (v^R_x\cos(\theta) + v^R_y\cos(90+\theta)) + (v^I_x\cos(\theta) + v^I_y\cos(90+\theta))i \ , \tag{5.14}$$
$$E_y = (v^R_x\cos(90-\theta) + v^R_y\cos(\theta)) + (v^I_x\cos(90-\theta) + v^I_y\cos(\theta))i \ . \tag{5.15}$$

Chapter 6

Numerical Results

In Chapter 5, we presented the experimental setup and the modelling equations for the numerical computations. In order to discuss the sensitivity of the electromagnetic signal with respect to an erroneous representation of the location and orientation of the receivers, we will in this chapter consider various experiments. In some of the experiments, we have used Gaussian distributed perturbations from the reference location or orientation with expected value $e = 0$ and some standard deviation s_t. To avoid unreasonably large perturbations, every perturbation below $-s_t$ and above s_t is set to $-s_t$ and s_t respectively.

6.1 Notation

For simplicity, we define some notation

$$\begin{aligned}
\Delta\hat{A}(F_j) &= \frac{|\delta\hat{A}(F_j)|}{\hat{A}(F_j^{(i)})}\,, \\
\Delta A(F_j) &= \frac{|\delta A(F_j)|}{A(F_j^{(i)})}\,, \\
\Delta\epsilon_A(F_j) &= |\frac{\delta\epsilon_A(F_j)}{\hat{A}(F_j^{(i)})}|\,, \\
\epsilon_A^r(F_j) &= |\frac{\hat{A}(F_j) - A(F_j)}{\hat{A}(F_j)}|\,,.
\end{aligned}$$

Here $\Delta\hat{A}(F_j)$ denotes the amplitudes of relative time-lapse signal computed for the reference location and orientation of the receivers, $\Delta A(F_j)$ denotes the amplitudes of relative time-lapse signal computed for the true location

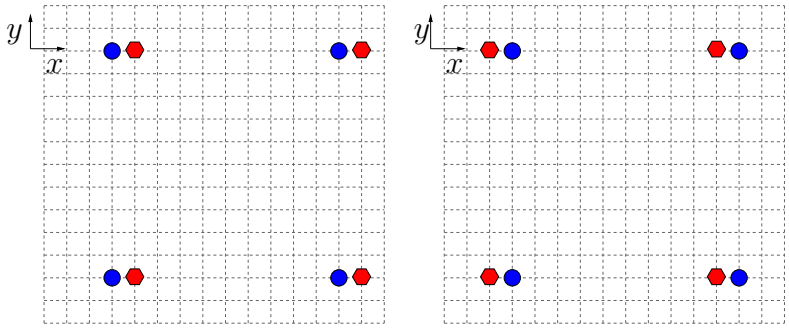

(a) Before flooding (b) After flooding

Figure 6.1: Visualization of the reference location in blue and the true location in red of the receivers seen from above. We notice the systematic perturbation of ± 10 m for every receiver.

or orientation of the receivers, $\Delta\epsilon_A(F_j)$ denotes the relative time-lapse errors of the amplitudes, and $\epsilon_A^r(F_j)$ denotes the relative modelling errors of the amplitudes.

6.2 Uncertainty in the Location of the Receivers

Let us now start by investigating how the components of the electromagnetic time-lapse signal will react on perturbations in the location of the receivers.

6.2.1 Experiment 1: Perturbation along the x-axis

In the first experiment we assume the true depth of the receivers to be 998 m constantly, and we systematically perturb the location of every receiver along the x-axis with $+10$ m before flooding and -10 m after flooding of the reservoir. The experimental setup of the location of the receivers is illustrated in Figure 6.1. In order to investigate the sensitivity of the components, we want to compare $\Delta A(F_j)$ computed for the true location of the receivers to $\Delta\hat{A}(F_j)$ computed for the reference location of the receivers. For this reason we have also plotted $\Delta\epsilon_A(F_j)$. For every electromagnetic component $\Delta\hat{A}(F_j)$, $\Delta A(F_j)$, and $\Delta\epsilon_A(F_j)$ will be presented as a function of receiver location.

The results for the electric components are shown in Figure 6.3. For the electric x-component, we see that $\Delta\hat{A}(E_x)$ and $\Delta A(E_x)$ are visible in a relatively broad region and that $\Delta A(E_x)$ is not completely masked by

$\Delta\epsilon_A(E_x)$. In the plots of the electric y-component, we see that both $\Delta\hat{A}(E_y)$ and $\Delta A(E_y)$ are visible for receivers located near $x = -3000$ m only, and that $\Delta A(E_y)$ are almost totally masked by $\Delta\epsilon_A(E_y)$. When it comes to the electric z-component, we will notice that $\Delta\hat{A}(E_z)$ and $\Delta A(E_z)$ is visible for almost every receiver, and that $\Delta\epsilon_A(E_z)$ is visible for receivers located near $x = -3000$ m only. This means that the influence of $\Delta\epsilon_A(E_z)$ on $\Delta A(E_z)$ will be small for a broad region of receivers. In the further investigation, we therefore want to focus on the electric x-component and the electric z-component.

The results for the magnetic components are shown in Figure 6.4. Let us first consider the magnetic x-component and the magnetic y-component. The plots of these components show that $\Delta\hat{A}(H_j)$ and $\Delta A(H_j)$ are visible in a relatively broad region and that for many receivers $\Delta A(H_j)$ will not be completely masked by $\Delta\epsilon_A(H_j)$. When it comes to the magnetic z-component, $\Delta\hat{A}(H_z)$ is not visible for any receiver, and it seems like $\Delta A(H_z)$ consist of errors only. We will therefore not consider the magnetic z-component any further in this study. Instead, we want to investigate the magnetic x- and y-components.

6.2.2 Experiment 2: Perturbation in the (x,y)-plane

In order to obtain a more realistic picture, each perturbation will now be a vector in the (x, y)-plane. The vectors are generated by two Gaussian distributed components for the x-axis and the y-axis. The standard deviation is in this experiment set to $s_t = 10$ m. We will still assume the depth of the receivers to be 998 m constantly, and the experimental setup of the receivers is illustrated in Figure 6.2.

The results are shown in Figure 6.5. We do notice the irregularities in the contours of $\Delta\epsilon_A(F_j)$ and $\Delta A(F_j)$ caused by the Gaussian distributed errors. For the electric x-component, we observe that the distribution of the relative time-lapse error $\Delta\epsilon_A(E_x)$ partly aligns with the relative time-lapse signal of the mathematical reference model, $\Delta\hat{A}(E_x)$. However, for the receivers located in the area $x = [2000, 6000]$, $y = [-5000, 5000]$, $\Delta A(E_x)$ will not be masked by $\Delta\epsilon_A(E_x)$. When it comes to the electric z-component, $\Delta\epsilon_A(E_z)$ is visible in receivers close to the source only. A relatively high signal to noise ratio is therefore displayed in most of the receivers. In the magnetic x-component, $\Delta\epsilon_A(E_x)$ are concentrated along the horizontal line of $y = 0$ m and along the vertical line of $x = -3000$ m, and in many receivers $\Delta\epsilon_A(E_x)$ do not mask $\Delta A(E_x)$. For the magnetic y-component, only small amounts of $\Delta\epsilon_A(E_x)$ are located in the region $x = [0, 4000]$, $y = [-5000, 5000]$. Since

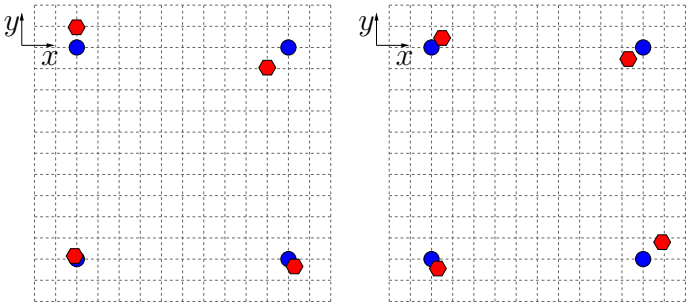

(a) Before flooding (b) After flooding

Figure 6.2: The plots visualize the reference location in blue and the true location in red of the receivers seen from above. The deviations from the reference locations are Gaussian distributed.

$\Delta A(H_y)$ measured by the receivers in this region is relatively strong, we will obtain a high signal-to-noise ratio here.

6.2.3 Experiment 3: Perturbation in the depth of the Sea-floor

In this experiment the perturbations in the (x, y)-plane are similar to those in the second experiment. However, the depth of the sea-floor and correspondingly the depth of the receivers will be perturbed systematically. It would be reasonable to assume that the variation in height of the sea-floor at these depths is smooth and that it over a small horizontal distance will be small. The depth of the sea-floor is therefore set to 1000 m in the acquisition before flooding of the reservoir and to 995 m in the acquisition after flooding of the reservoir. The corresponding depths of the receivers are then 999 m before flooding and 994 m after flooding.

The results are shown in Figure 6.6. If we compare the results with the results in experiment 2, we will see that the perturbation of the depth of the sea-floor will have small influence on the signals. This applies for all components.

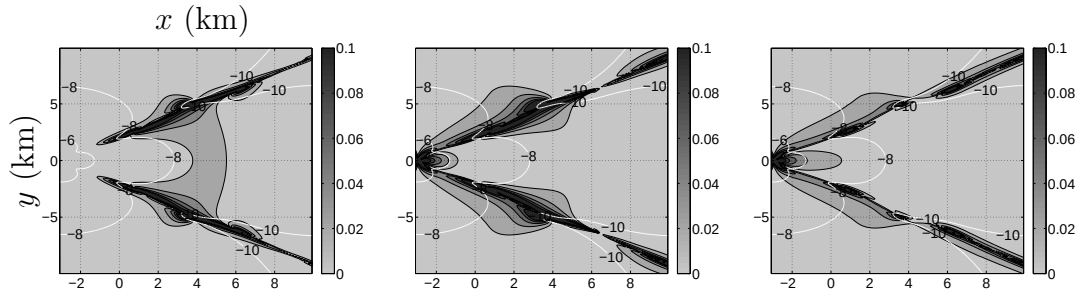

(a) The numerical results obtained from computations of E_x.

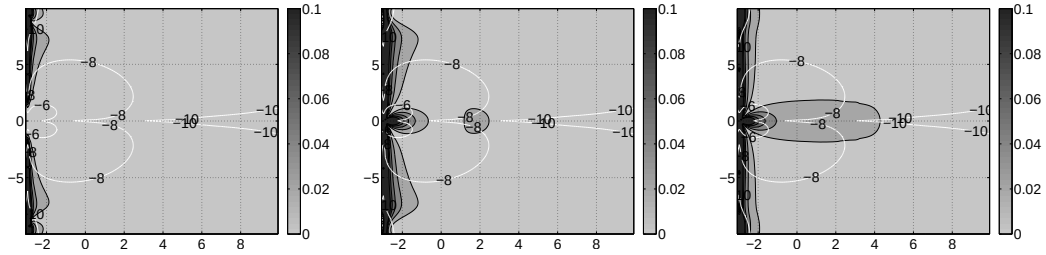

(b) The numerical results obtained from computations of E_y.

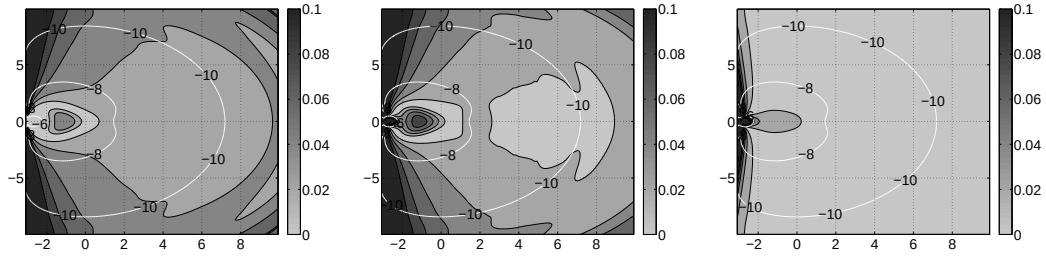

(c) The numerical results obtained from computations of E_z.

Figure 6.3: Left-hand column: $\Delta\hat{A}(E_j)$ computed for the reference location of the receivers. Mid column: $\Delta A(E_j)$ computed for the true location of the receivers. Right-hand column: shows $\Delta\epsilon_A(E_j)$. All values are plotted as a function of the position (in km). The white contours in the plots of $\Delta\hat{A}(E_j)$ and $\Delta\epsilon_A(E_j)$ show $\log\hat{A}(E_j)$, and in the plots of $\Delta A(E_j)$ they show $\log A(E_j)$. These contour lines gives the magnitude of the strength of the fields at each time instance. This applies for all similar figures.

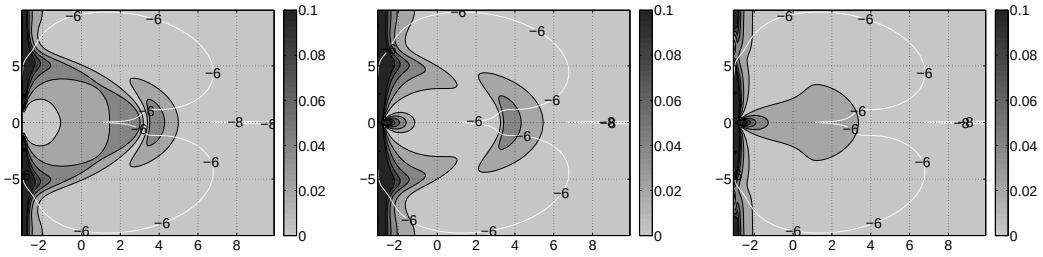

(a) The numerical results obtained from computations of H_x.

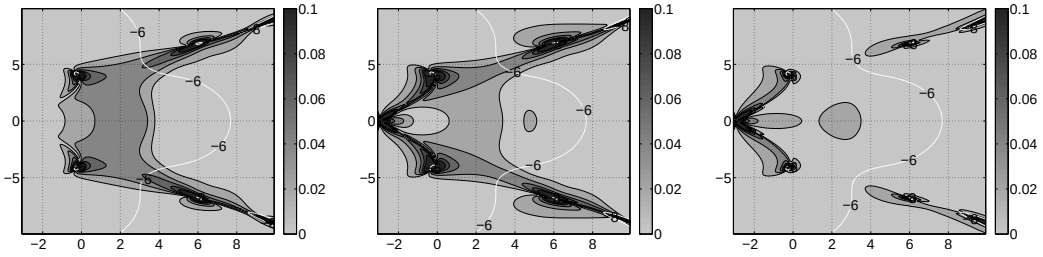

(b) The numerical results obtained from computations of H_y.

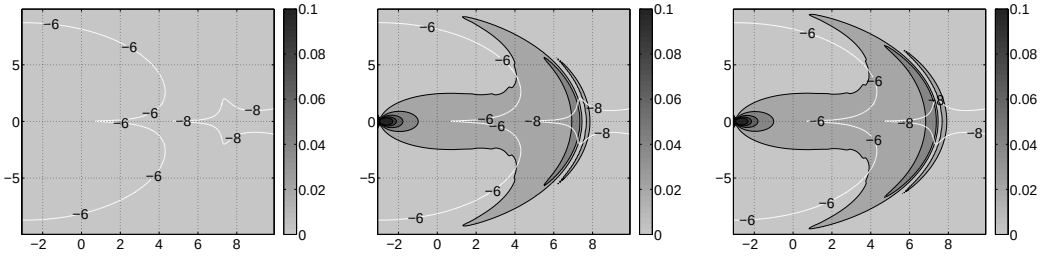

(c) The numerical results obtained from computations of H_z.

Figure 6.4: Left-hand column: $\Delta\hat{A}(H_j)$. Mid column: $\Delta A(H_j)$. Right-hand column: $\Delta\epsilon_A(H_j)$.

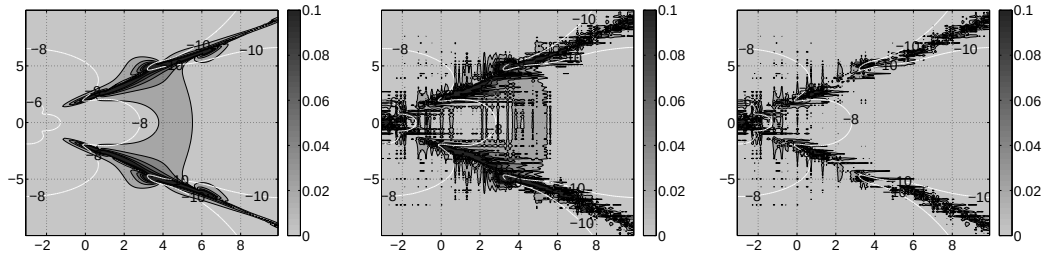

(a) The numerical results obtained from computations of E_x.

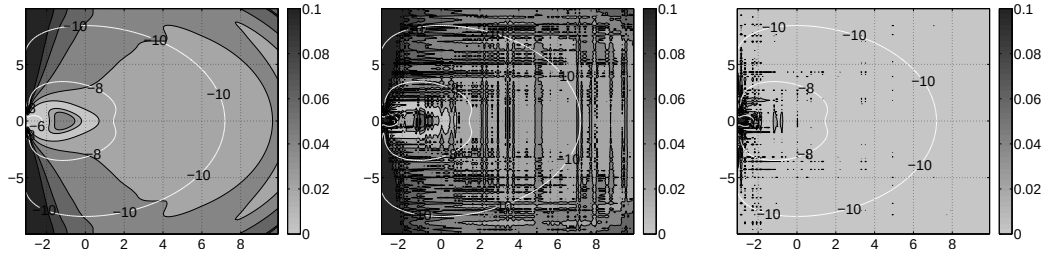

(b) The numerical results obtained from computations of E_z.

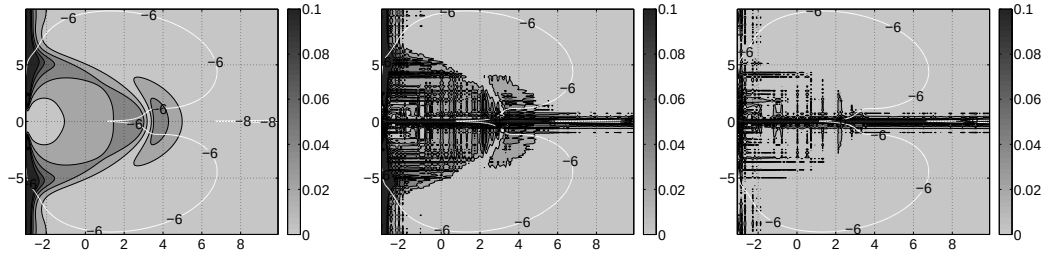

(c) The numerical results obtained from computations of H_x.

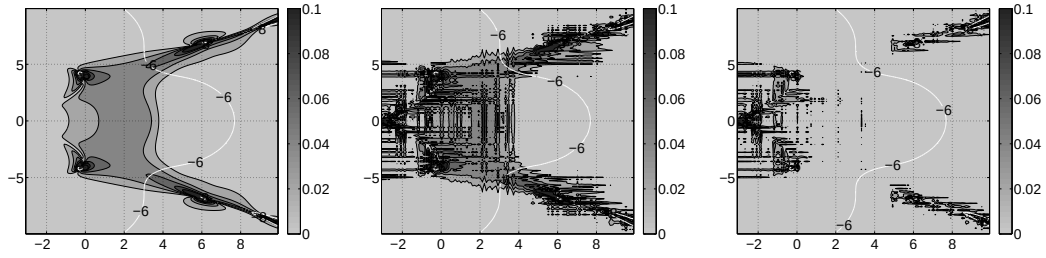

(d) The numerical results obtained from computations of H_y.

Figure 6.5: Left-hand column: $\Delta\hat{A}(F_j)$. Midcolumn: $\Delta A(F_j)$. Right-hand column: $\Delta\epsilon_A(F_j)$.

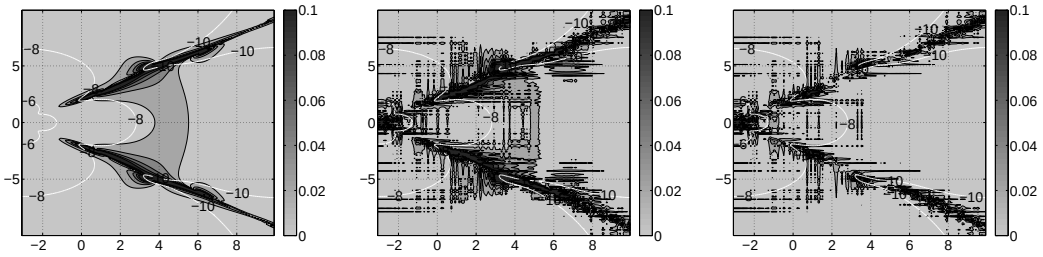

(a) The numerical results obtained from computations of E_x.

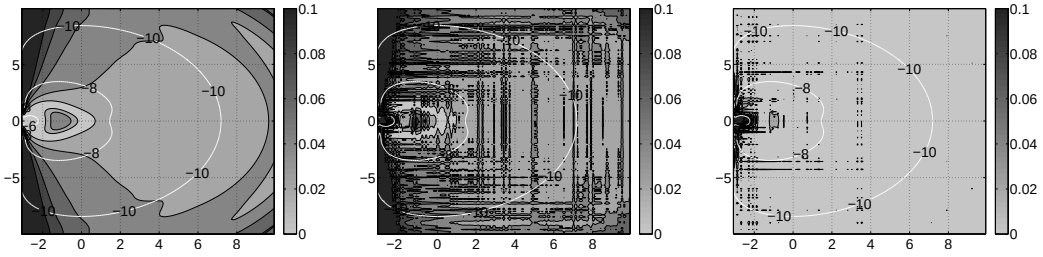

(b) The numerical results obtained from computations of E_z.

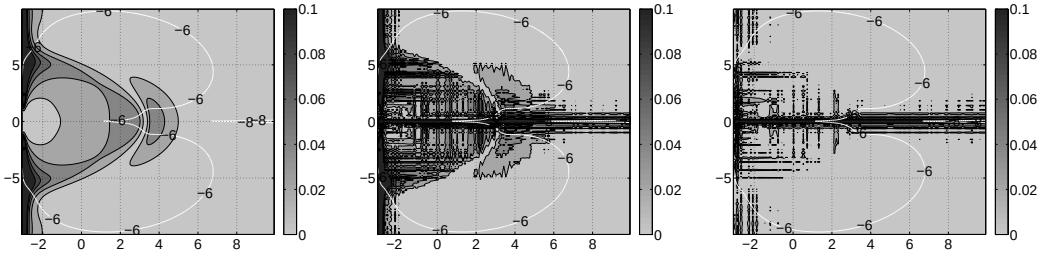

(c) The numerical results obtained from computations of H_x.

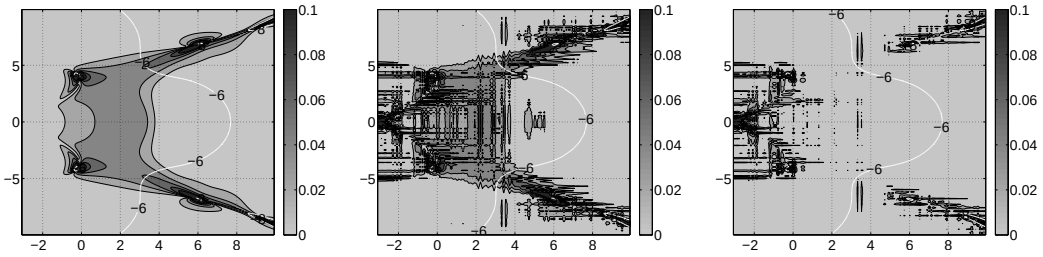

(d) The numerical results obtained from computations of H_y.

Figure 6.6: Left-hand column: $\Delta\hat{A}(F_j)$. Mid column: $\Delta A(F_j)$. Right-hand column: $\Delta\epsilon_A(F_j)$.

6.3 Tilting of the Receivers in the (x, z)-plane

Uncertainty in the tilting of the receivers may be caused by an erroneous representation of the slope of the sea-floor. We will denote the angle between the reference sea-floor and the true sea-floor β. See Figure 6.7. Since the slope of the true sea-floor may change with the position $\boldsymbol{x}$, uncertainties in the orientation may also arise as a result of the erroneous representation of the location of the receivers. We will denote the angular deviation between the slope of the sea-floor at the reference location and the slope at the true location α. The angular deviation α is shown in Figure 6.8

Recall that we have assumed the variation in depth of the sea-floor to be be small over a small horizontal distance and the maximum deviation from the reference location of the receivers to be ± 10 m. Most likely, α will therefore not be large.

6.3.1 Experiment 1: Investigation of the Electric z-component

In this experiment we will investigate the sensitivity of the electric z-component with respect to tilting in the (x, z)-plane. For this investigation, results for various perturbations will be shown.

Example 1

We will now first assume that the x-axis of the reference orientation is parallel to a completely horizontal sea-floor. This means that $\beta = 0$. For simplicity we further assume that the true orientation of the receivers before flooding of the reservoir coincide with the reference orientation. The true orientations of the receivers after flooding is taken to differ from the reference orientation with a Gaussian distributed angular deviations α. We will now observe how $\Delta A(E_z)$ reacts to increasing values of α. The results for standard deviations $s_t^\alpha = 0^\circ$, $s_t^\alpha = 0.1^\circ$, $s_t^\alpha = 0.2^\circ$, and $s_t^\alpha = 0.3^\circ$ are shown in Figure 6.10.

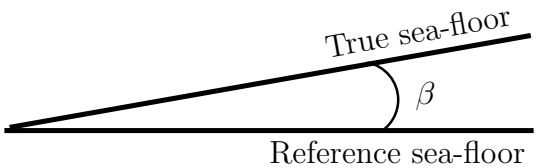

Figure 6.7: Illustration of the angular deviation, β, between the reference sea-floor and the true sea-floor.

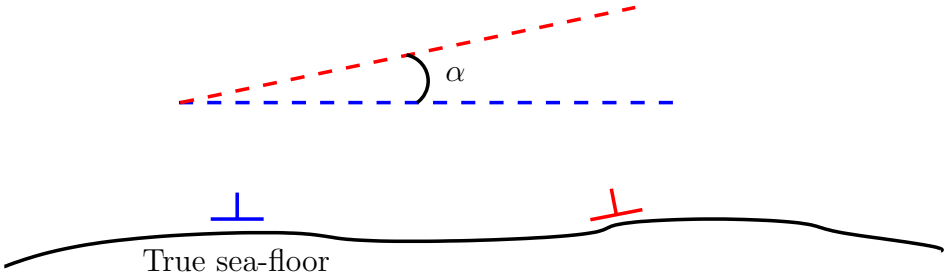

Figure 6.8: The angular deviation, α, between the receiver located at the reference position and the receiver located at the true position.

From the plots, we see that $\Delta A(E_z)$ is extremely sensitive to perturbations in α. For values as low as $s_t^\alpha = 0.3$, $\Delta A(E_z)$ is almost completely masked by $\Delta\epsilon_A(E_z)$. The high sensitivity is caused by the large difference in magnitude between $\hat{A}(E_x)$ and $\hat{A}(E_z)$. Let us consider Figure 6.9. The white contour lines shown in the figure gives the magnitude of the strength of the fields. If we notice the different shape of these contours, we see that the magnitude of $\hat{A}(E_z)$ is less than the magnitude of $\hat{A}(E_x)$ for many receivers. Typically, $E_{x'}$ is 10-100 times larger than $E_{z'}$. For this reason, the contribution from $E_{x'}$ in equation (5.13) will be large, and thus a very small tilting of the receivers will cause $\Delta A(E_z)$ to be masked by $\Delta\epsilon_A(E_z)$.

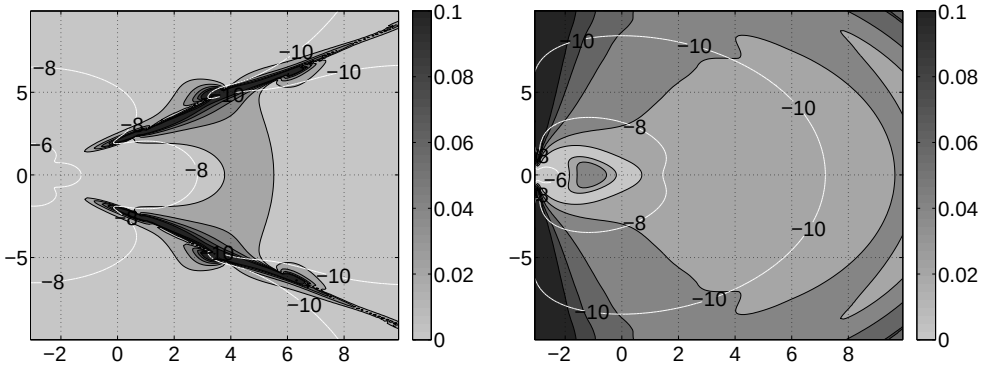

Figure 6.9: The left-hand plot: shows $\Delta\hat{A}(E_x)$, and the white contours are $\log \hat{A}(E_x)$. The right-hand plot: shows $\Delta\hat{A}(E_z)$ and the white contours are $\log \hat{A}(E_z)$. Notice the different shape of $\log \hat{A}(E_x)$ and $\log \hat{A}(E_z)$

Example 2

Let us further observe how $\delta P(E_z)$ reacts to similar perturbations. In Figure 6.11 the results for standard deviations $s_t^\alpha = 0^\circ$, $s_t^\alpha = 0.2^\circ$, $s_t^\alpha = 0.5^\circ$, and $s_t^\alpha = 1^\circ$ are shown.

Compared to $\Delta A(E_z)$, $\delta P(E_z)$ is less sensitive to perturbations in α. Anyway, $\delta P(E_z)$ is almost completely masked by $\delta\epsilon_P(E_z)$ for values as low as $\alpha = 1^\circ$. We see that $\delta\epsilon_P(E_z)$ displays a similar tendency as $\Delta\epsilon_A(E_z)$, and that in areas of weak $\hat{A}(E_x)$, $\delta\epsilon_P(E_z)$ is low.

Example 3

In the following example we assume that the true sea-floor is perturbed with $\beta = 10^\circ$ from the reference sea-floor. Additionally, the orientation of the receivers in the acquisition after flooding of the reservoir has been perturbed with a small Gaussian distributed deviation, α. In this example results for $s_t^\alpha = 0.1^\circ$ are shown in Figure 6.12.

Since the perturbation β before and after flooding is equal, we will expect some cancellation from $\epsilon_{\hat{A}}(E_z)$ to $\Delta\epsilon_A(E_z)$. If we compare the upper and lower right-hand plot, the cancellation is easily seen. Nevertheless, $\Delta A(E_z)$ is almost completely masked by $\Delta\epsilon_A(E_z)$ for α with $s_t = 0.1^\circ$.

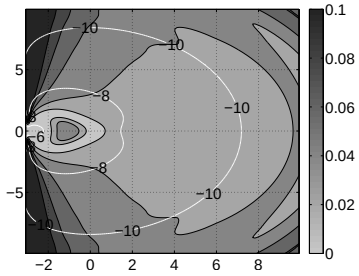

(a) Angular deviation $\alpha = 0°$.

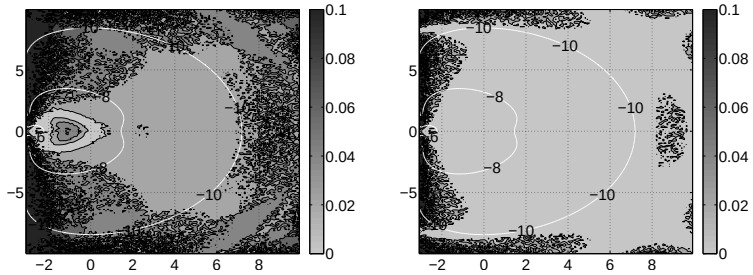

(b) Angular deviation with $s_t^\alpha = 0.1°$.

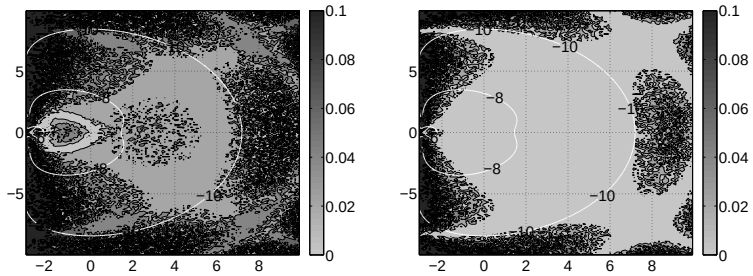

(c) Angular deviation with $s_t^\alpha = 0.2°$.

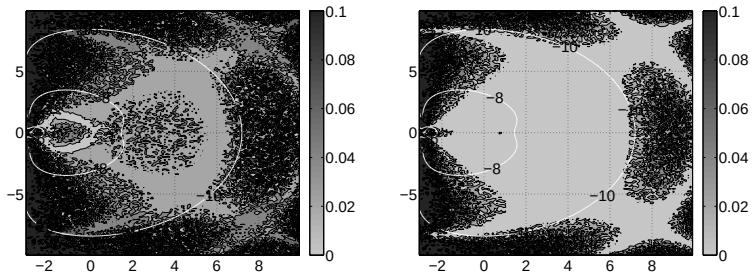

(d) Angular deviation with $s_t^\alpha = 0.3°$.

Figure 6.10: Upper plot: $\Delta\hat{A}(E_z)$ computed for the reference orientation of the receivers. Left-hand column: $\Delta A(E_z)$ computed for the true orientation of the receivers. Right-hand column: $\Delta\epsilon_A(E_z)$. The perturbations are increased downwards.

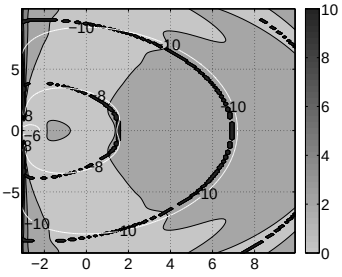

(a) Angular deviation $\alpha = 0°$.

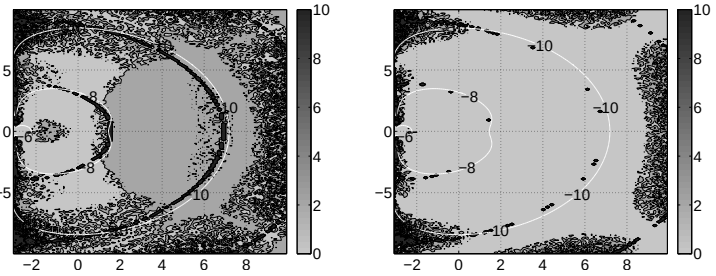

(b) Angular deviation with $s_t^\alpha = 0.2°$.

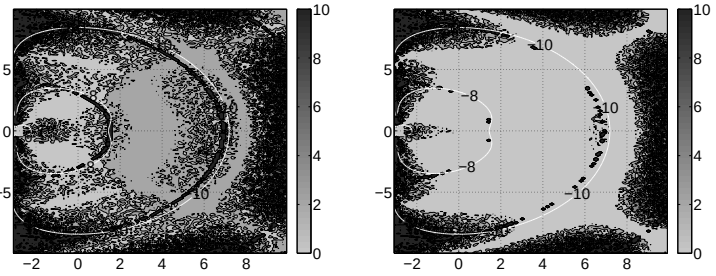

(c) Angular deviation with $s_t^\alpha = 0.5°$.

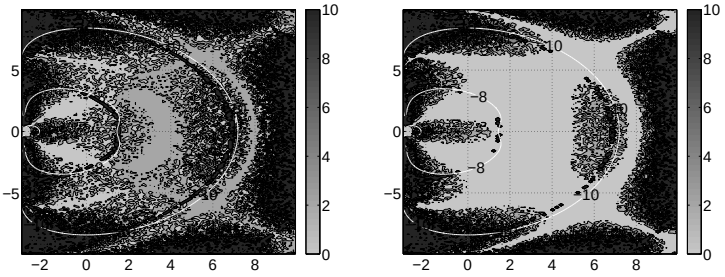

(d) Angular deviation with $s_t^\alpha = 1°$.

Figure 6.11: Upper plot: $\delta\hat{P}(E_z)$ computed for the reference orientation of the receivers. Left-hand column: $\delta P(E_z)$ computed for the true orientation of the receivers. Right-hand column: $\delta\epsilon_P(E_z)$. The perturbations are increased downwards. The white contours in the plots of $\delta\hat{P}(E_z)$ and $\delta\epsilon_P(E_z)$ show $\log\hat{A}(E_z)$, and in the plots of $\Delta P(E_z)$ they show $\log A(E_z)$. This applies for similar phase plot.

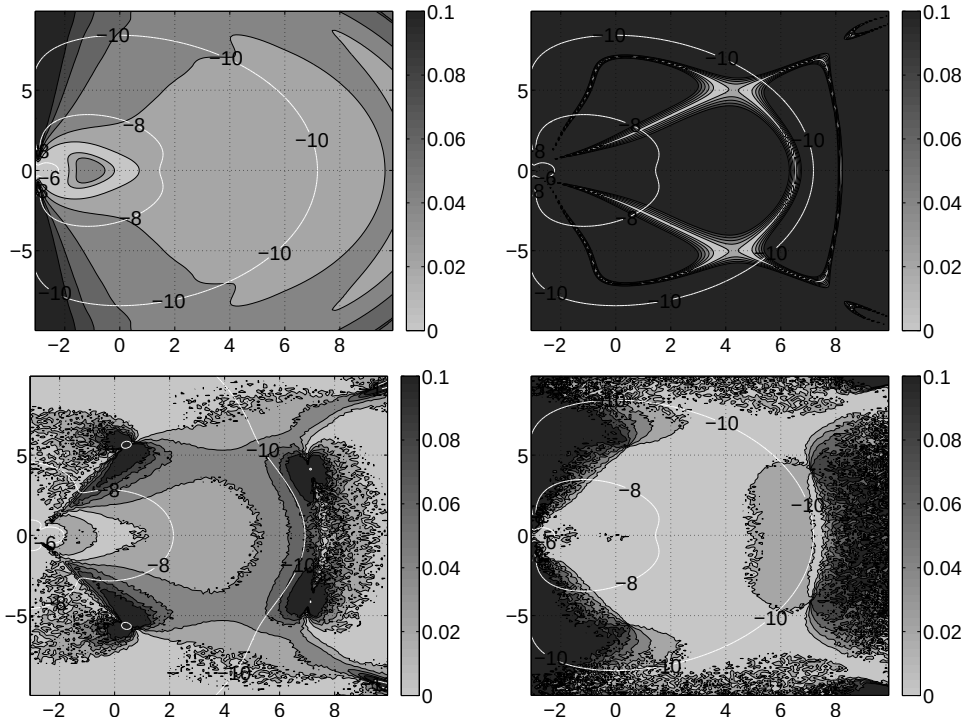

Figure 6.12: The upper left-hand plot: $\Delta\hat{A}(E_z)$ for the reference orientation of the receivers. The lower left-hand plot: $\Delta A(E_z)$ for the true orientation of the receivers. The upper right-hand plot: $\epsilon_A^r(E_z)$. The lower right-hand plot: $\Delta\epsilon_A(E_z)$. The white contours in the plots of $\Delta A(E_z)$ show $\log A(E_z)$, and in the plots of $\Delta\hat{A}(E_z)$, $\epsilon_A^r(E_z)$, and $\Delta\epsilon_A(E_z)$ show $\log \hat{A}(E_z)$.

6.3.2 Experiment 2: Investigation of the Electric x-component

Example 1

As for E_z, we will start the investigation of the electric x-component by assuming that the true sea-floor coincide with the reference sea-floor so that $\beta = 0$. In the acquisition after flooding, the receivers are perturbed with a small Gaussian distributed deviation α. The results for standard deviation $s_t^\alpha = 0^\circ$, $s_t^\alpha = 1^\circ$, $s_t^\alpha = 3^\circ$, and $s_t^\alpha = 5^\circ$ are shown in Figure 6.13.

Compared to $\Delta A(E_z)$, $\Delta A(E_x)$ is less sensitive. However, for standard deviation of α grater than $s_t^\alpha \approx 5^\circ$, $\Delta A(E_x)$ will be almost completely masked by $\Delta\epsilon_A(E_x)$. We notice that the errors are aligned with the signal. The reason is that E_x is low compared to E_z in these regions. See Figure 6.9. For this

reason, the contribution from $E_{z'}$ in equation (**??**) will be large, and thus a small tilting of the receivers will cause $\Delta A(E_x)$ to be masked by $\Delta\epsilon_A(E_x)$.

Example 2

Let us observe how $\delta P(E_x)$ reacts at similar perturbations. In Figure 6.14 the results for standard deviations $s_t^\alpha = 0^\circ$, $s_t^\alpha = 1^\circ$, $s_t^\alpha = 5^\circ$, and $s_t^\alpha = 10^\circ$ are shown.

Relative to $\Delta A(E_x)$, $\delta P(E_x)$ is less sensitive to perturbations in the orientation of the receivers. As for $\Delta A(E_x)$ the errors are aligned with the signal. It may, however, be possible to extract some information for receivers located in the area about $x = [0, 2000]$ m, $y = [-2000, 2000]$ m. Nevertheless, $\delta P(E_x)$ is relatively weak in this area, and obtaining useful information may be difficult.

Example 3

We now assume that $\beta = 10^\circ$. Additionally, the orientation of the receivers in the acquisition after flooding of the reservoir has been perturbed with a small Gaussian distributed deviation, α with standard deviation $s_t^\alpha = 2^\circ$. The results are shown in Figure 6.15.

As for the similar experiment for $A(E_x)$, cancellation from $\epsilon_{\hat{A}}(E_x)$ to $\Delta\epsilon_A(E_x)$ is expected. The cancellation is easily seen, if we compare the upper and lower right-hand plots. The small perturbation α will, however, cause $\Delta A(E_x)$ to be almost completely masked by $\Delta\epsilon_A(E_x)$ for perturbations greater than $\alpha \approx 2^\circ$.

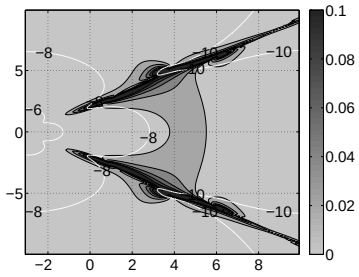

(a) Angular deviation $\alpha = 0°$.

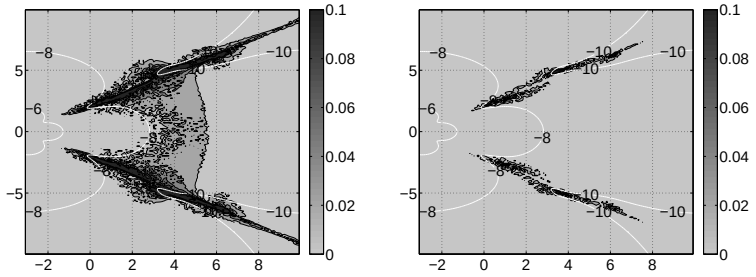

(b) Angular deviation with $s_t^\alpha = 1°$.

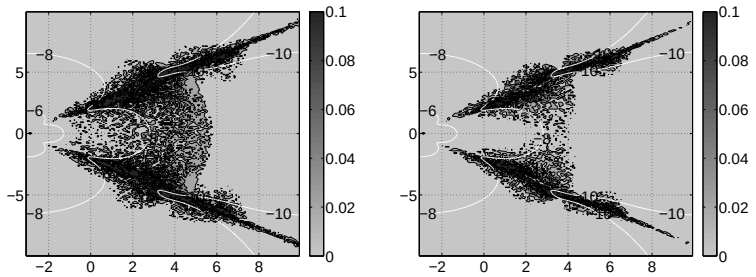

(c) Angular deviation with $s_t^\alpha = 3°$.

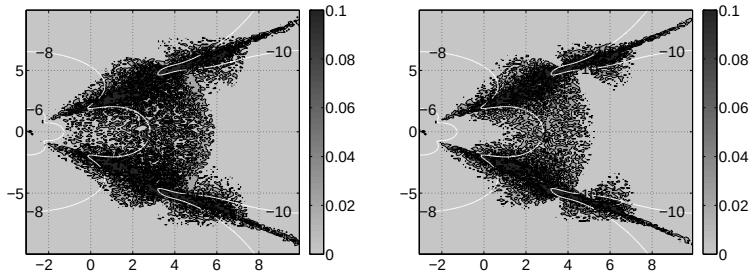

(d) Angular deviation with $s_t^\alpha = 5°$.

Figure 6.13: Upper plot: $\Delta\hat{A}(E_x)$. Left-hand column: $\Delta A(E_x)$. Right-hand column: $\Delta\epsilon_A(E_x)$.

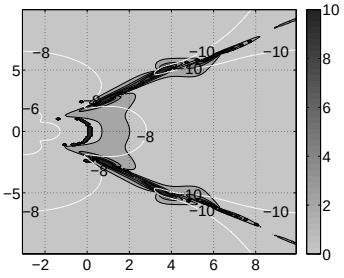

(a) Angular deviation $\alpha = 0°$.

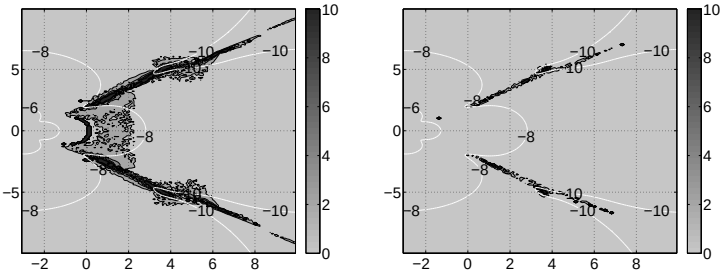

(b) Angular deviation with $s_t^\alpha = 1°$.

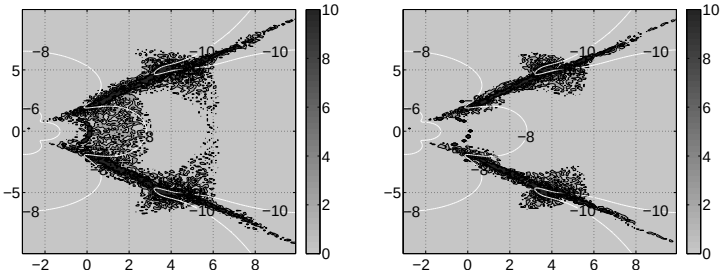

(c) Angular deviation with $s_t^\alpha = 5°$.

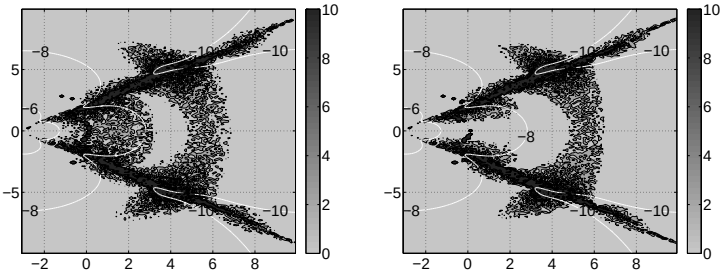

(d) Angular deviation with $s_t^\alpha = 10°$.

Figure 6.14: Upper plot: $\delta\hat{P}(E_x)$. Left-hand column: $\delta P(E_x)$. Right-hand column: $\delta\epsilon_P(E_x)$. The perturbations are increased downwards. The white contours in the plots of $\delta\hat{P}(E_x)$ and $\delta\epsilon_P(E_x)$ show $\log\hat{A}(E_x)$, and in the plots of $\Delta P(E_x)$ they show $\log A(E_x)$.

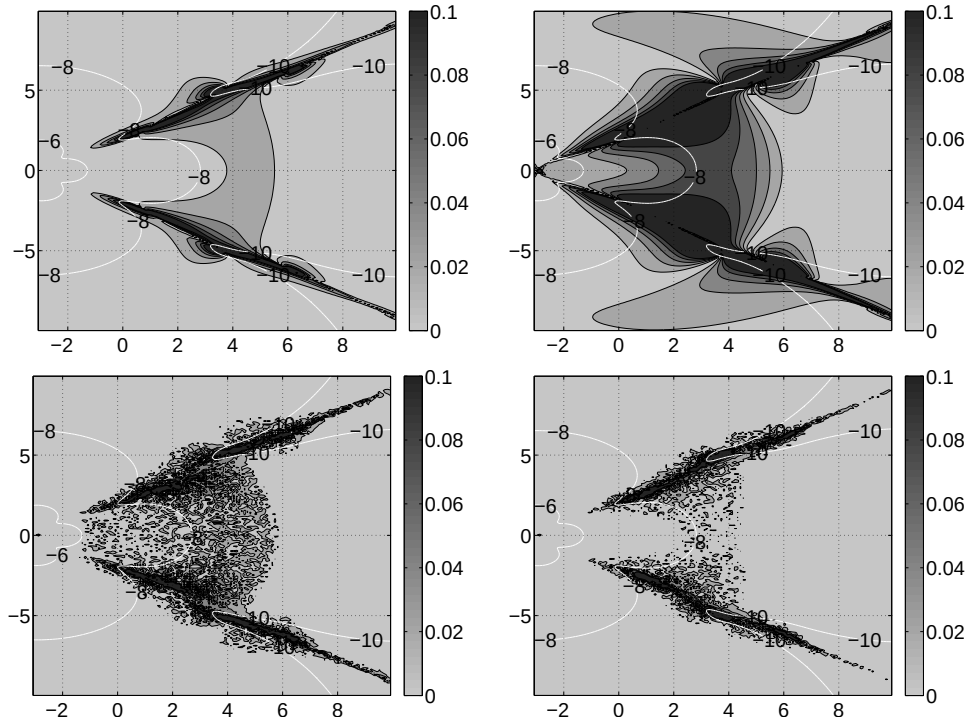

Figure 6.15: The upper left-hand plot: shows $\Delta\hat{A}(E_x)$ for the reference orientation of the receivers. The lower left-hand plot: $\Delta A(E_x)$. The upper right-hand plot: $\epsilon_A^r(E_x)$. The lower right-hand plot: $\Delta\epsilon_A(E_x)$. The white contours in the plots of $\Delta A(E_x)$ show $\log A(E_x)$, and in the plots of $\Delta\hat{A}(E_x)$, $\epsilon_A^r(E_x)$, and $\Delta\epsilon_A(E_x)$ show $\log\hat{A}(E_x)$.

6.4 Horizontal Rotation of the Receivers

Example 1: Amplitude

For rotation of the receivers in the (x, y)-plane, it will be reasonable to assume that the angular deviation, ψ, from the reference orientation is Gaussian distributed. The results for standard deviations $s_t^\psi = 0^\circ$, $s_t^\psi = 0.1^\circ$, $s_t^\psi = 0.5^\circ$, and $s_t^\psi = 1^\circ$ are shown in Figure 6.17.

Compared to the tilting case, we observe that $\Delta A(E_x)$ is even more sensitive to horizontal rotation of the receivers, and this is caused by the large difference in magnitude between $\hat{A}(E_x)$ and $\hat{A}(E_y)$. Let us consider Figure 6.16. The magnitude of $\hat{A}(E_y)$ is typically of magnitude $10 - 100$ times greater than $\hat{A}(E_x)$ for the areas with large values of $\Delta A(E_x)$. For this reason, $\Delta A(E_x)$ is almost completely masked by $\Delta\epsilon_A(E_x)$ for standard deviations of

ψ larger than $s_t^\psi \approx 1$.

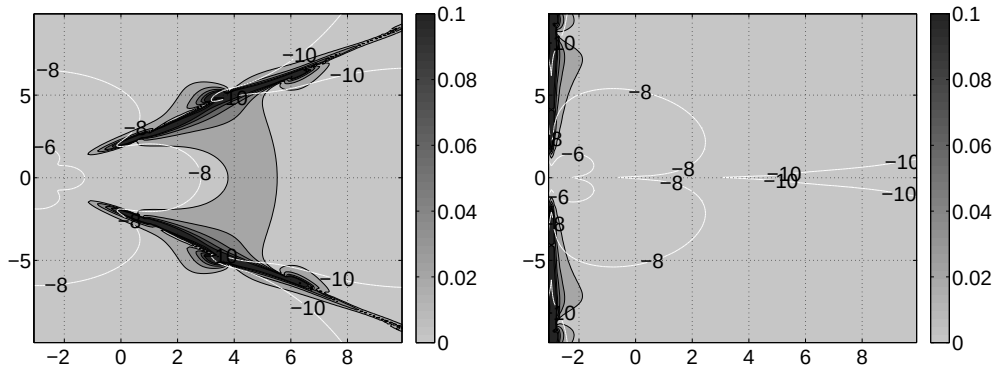

(a) The numerical results obtained from computations of E_x.

Figure 6.16: Left-hand plot: $\Delta\hat{A}(E_x)$ and white contours $\log \hat{A}(E_x)$. Right-hand plot: $\Delta\hat{A}(E_y)$ and white contours $\log \hat{A}(E_y)$. Notice the various shape of $\log \hat{A}(E_x)$ and $\log \hat{A}(E_y)$

Example 2: Phase

Let us observe how $\delta P(E_x)$ reacts at similar perturbations. The results for standard deviations $s_t^\psi = 0^\circ$, $s_t^\psi = 1^\circ$, $s_t^\psi = 5^\circ$, and $s_t^\psi = 10^\circ$ are shown in Figure 6.18.

Compared to $\Delta A(E_x)$, $\delta P(E_x)$ is less sensitive to horizontal rotation of the receivers. Nevertheless, $\delta\epsilon_P(E_x)$ aligns with $\delta P(E_x)$, and only relatively a small area $x \approx [0, 2000]$ m, $y \approx [-2000, 2000]$ is not covered. The signal, $\delta P(E_x)$, in this region is, however, relatively weak, and it may be difficult to extract information about the changes in the conductivity distribution.

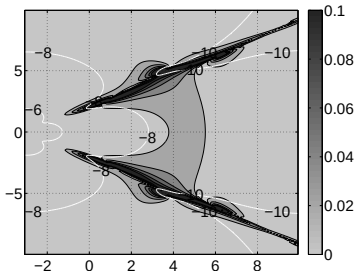

(a) Angular deviation $s_t^{\psi} = 0^{\circ}$.

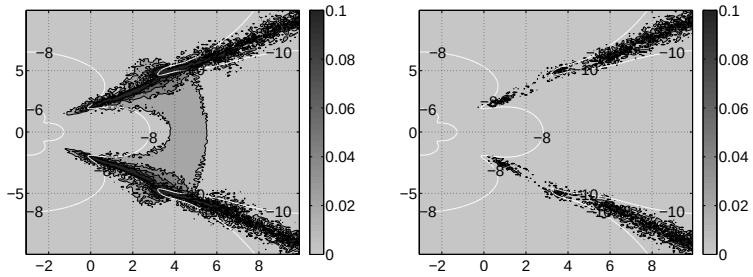

(b) Angular deviation $s_t^{\psi} = 0.1^{\circ}$.

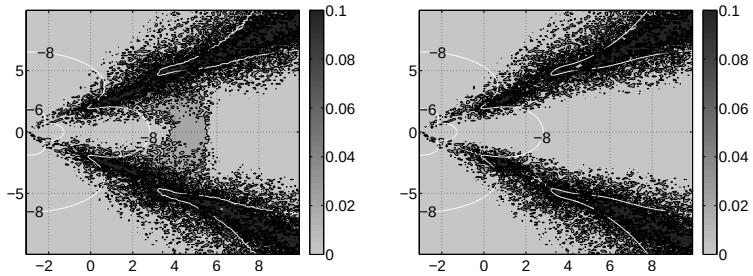

(c) Angular deviation $s_t^{\psi} = 0.5^{\circ}$.

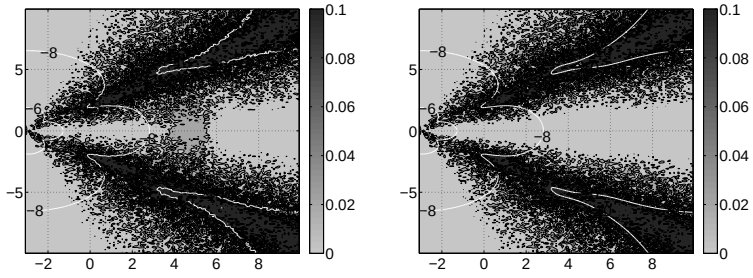

(d) Angular deviation $s_t^{\psi} = 1^{\circ}$.

Figure 6.17: The upper plot shows $\Delta\hat{A}(E_x)$ computed for the reference orientation of the receivers. Underneath this plot, the left-hand column shows $\Delta A(E_x)$ computed for the true orientation of the receivers, and the right-hand column shows $\Delta\epsilon_A(E_x)$. The perturbations are increased downwards.

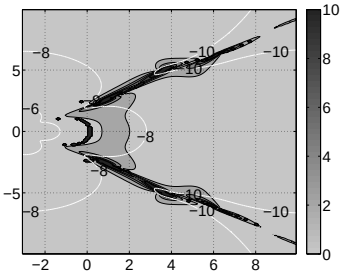

(a) Angular deviation $s_t^{\psi} = 0^{\circ}$.

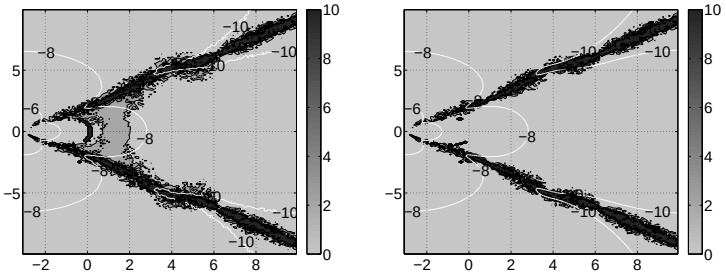

(b) Angular deviation $s_t^{\psi} = 1^{\circ}$.

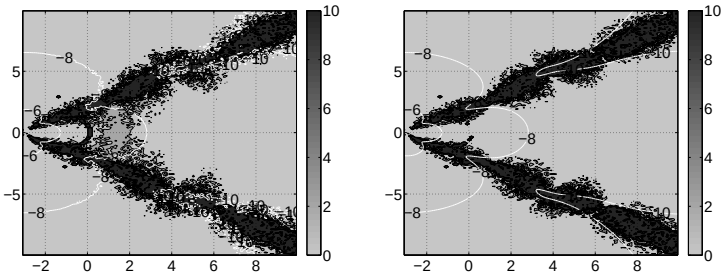

(c) Angular deviation $s_t^{\psi} = 5^{\circ}$.

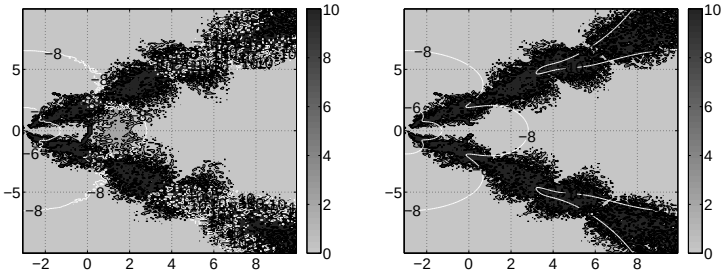

(d) Angular deviation $s_t^{\psi} = 10^{\circ}$.

Figure 6.18: The upper plot shows $\delta\hat{P}(E_x)$ computed for the reference orientation of the receivers. Underneath this plot, the left-hand column shows $\delta P(E_x)$ computed for the true orientation of the receivers, and the right-hand column shows $\delta\epsilon_P(E_x)$. The perturbations are increased downwards.

Chapter 7

Summary, Conclusion, and Further Work

CSEM waves are highly influenced by the electric conductivity distribution of the media in which it propagates. In a porous medium, the electric conductivity is closely related to the fluid saturation. Since a porous rock saturated with hydrocarbons displays a considerably lower electric conductivity than a porous rock saturated with saline water, CSEM data can be applied to discriminate between saline water and hydrocarbons in the subsurface. As it comes to production monitoring, changes in the measured electromagnetic field over time may be used to determine the evolution of the front that separates oil and saline water in the reservoir. In this thesis, the sensitivity of CSEM data with respect to prescribed perturbations in the location and orientation of the receivers has been investigated. The question is whether or not repeatedly replacement of the receivers in the succsessive aquisitions will destroy the electromagnetic time-lapse signal. The alternative may be to fix the receivers at the sea-floor.

Our experiments indicate that the time-lapse data are robust with respect to perturbations in the location, and repeatedly replacement of the receivers seems thus acceptable from this point of view. As an example, several components will tolerate a systematic perturbation of magnitude ± 10 m in the location of the receivers.

The CSEM time-lapse amplitude data investigated for E_x and E_z is extremely sensitive to perturbations due to tilting of the receivers in the (x, z)-plane. This is caused by the large difference in magnitude between E_x and E_z. The results for the time-lapse phase data seem somewhat more promising, but the area of receivers which is not completely masked by errors displays relatively low signals, and it may be difficult to extract information from these data. The CSEM time-lapse amplitude data investigated for E_x shows

a similar behaviour for horizontal rotations due to the large difference in magnitude between E_x and E_y.

Errors both in the location and orientation of the receivers must be anticipated. From the numerical experiments performed in this thesis we therefore conclude that fixed receivers in reservoir production monitoring seems necessary to obtain acceptable results. In further work it would be interesting to consider how the magnetic components will react to perturbations in the orientation of the receivers. Another interesting issue is to study the sensitivity of CSEM signals with respect to perturbations in the location and orientation of the source.

References

Boggs, S. (2006). *Principles of Sedimentology and Stratigraphy* (fourth ed.). Pearson Education, Inc. ISBN: 0-13-154728-3.

Eidesmo, T., S. Ellingsrud, A. Farestveit, H. M. Pedersen, and S. Johansen (2006, September). Method and apparatus for determining the nature of submarine reservoirs. *Patent Application Publication, Pub.No.: US 2006/0197532 A1*. PCT filed: March 2004.

Eidesmo, T., S. Ellingsrud, F.-N. Kong, H. Westerdahl, and S. Johansen (2004, July). Method and apparatus for determining the nature of subterranean reservoirs. *Patent Application Publication, Pub.No.: US 2004/0124842 A1*. Filed: July 2003.

Eidesmo, T., S. Ellingsrud, L. M. Macgregor, S. Constable, M. C. Sinha, S. Johansen, F. N. Kong, and H. Westerdahl (2002, March). Sea bed logging (sbl), a new method for remote and direct identification of hydrocarbon filled layers in deepwater areas. *First break 20*(3), 144–152.

Ellingsrud, S., T. Eidesmo, F.-N. Kong, and H. Westerdahl (2005, February). Method and apparatus for determining the nature of subterranean reservoirs using refracted electromagnetic waves. *US States Patent, Patent No.: US 6,859,038 B2*. Filed: April 2002.

Ellingsrud, S., T. Eidesmo, H. M. Pedersen, and T. Schaug-Pettersen (2006, May). Method and apparatus for determining the nature of subterranean reservoirs. *Patent Application Publication, Pub. No.: US 2006/0091889 A1*. Filed: December 2005.

Ellingsrud, S., T. Eidesmo, H. Westerdahl, and F.-N. Kong (2004, September). Electromagnetic method and apparatus for determining the nature of subterranean reservoirs using refracted electromagnetic waves. *Patent Application Publication, Pub.No.: US 2004/0176910 A1*. Filed: March 2004.

Flosadottir, A. H. and S. Constable (1996, March). Marine controlled-

source electromagnetic sounding, 1. modeling and experimental design. *Journal of geophysical research 101*(B3), 5507–5517.

Fowler, C. M. R. (2005). *The Solid Earth, An Introduction to Global Geophysics* (2nd ed.). Cambridge University Press. ISBN: 0 521 89307 0.

Gueguen, Y. and V. Palaciauskas (1994). *Introduction to the Physics of Rocks*. Princeton University Press. ISBN: 0-691-03452-4.

Hursan, G. and M. S. Zhdanov (2002). Contraction integral equation method in three-dimensional electromagnetic modeling. *Radio Science 37*(6).

Kundu, P. K. and I. M. Cohen (2004). *Fluid Mechanics*. Elsevier Academic Press. ISBN-10: 0-12-178253-0.

Lien, M. and T. Mannseth (2007). Sensitivity study of marine csem data for reservoir production monitoring.

Lien, M. and T. Mannseth (2008, July-August). Sensitivity study of marine csem data for reservoir production monitoring. *Geophysics 73*(4), F151–F163.

Malinverno, A. and C. Torres-Verdin (2000). Bayesian inversion of dc electrical measurements with uncertainties for reservoir monitoring. *Inverse Problems 16*, 1343–1356.

Marshak, S. (2001). *Earth: Portrait of a Planet* (first ed.). W. W. Norton and Company, Inc. ISBN: 0-393-97423-5.

Mavko, G., T. Mukerji, and J. Dvorkin (1998). *The Rock Physics Handbook - Tools for Seismic Analysis in Porous Media*. Cambridge University Press. ISBN: 0-521-54344-4.

Maxwell, J. C. (1864). A dynamical theory of the electromagnetic field. *Philosophical Transactions of the Royal Society of London 155*, 459–512.

Nesse, W. D. (2000). *Introduction to Mineralogy*. Oxford University Press. ISBN: 0-19-510691-1.

Orange, A., K. Key, and C. S. (2009). The feasibility of reservoir monitoring using time-lapse marine csem. *Geophysics 74*, F21–F29.

Pettersen, Ø. (1990). *Grunnkurs i reservoarmekanikk*. Matematisk institutt, Universitetet i Bergen.

Reitz, J. R., F. J. Milford, and R. W. Christy (1993). *Foundation of Electromagnetic Theory*. Addison-Wesley Publishing Company. ISBN: 0-201-52624-7.

Tipler, P. A. (1976). *Physics*. Worth Publishers, Inc. ISBN: 0-87901-041-X.

Tipler, P. A. and G. Mosca (2004). *Physics for Scientists and Engineers* (fifth ed.). W.H. Freeman and Company. ISBN: 0-7167-8339-8.

Webb, S. C., C. S. Constable, and C. S. Cox (1985). A seafloor electric field instrument. *Journal of Geomagnetism and Geoelectricity 37*, 1115–1129.

Wilt, M. and M. Morea (2004). 3d waterflood monitoring at lost hills with crosshole em. *The Leading Edge 23*, 489–493.

Zhdanov, M. (Ed.) (2002). *Geophysical Inverse Theory and Regularization Problems*. Elsevier.